

Engineering Miniband Topology via Band-Folding in Moiré Superlattice Materials

Kaijie Yang,^{1,*} Yunzhe Liu,^{1,*} Frank Schindler,² and Chao-Xing Liu^{1,†}

¹*Department of Physics, The Pennsylvania State University, University Park, Pennsylvania 16802, USA*

²*Blackett Laboratory, Imperial College London, London SW7 2AZ, United Kingdom*

(Dated: May 24, 2024)

The emergence of topologically non-trivial flat bands in moiré materials provides an opportunity to explore the interplay between topological physics and correlation effects, leading to the recent experimental realization of interacting topological phases, e.g. fractional Chern insulators. In this work, we propose a mechanism of band inversion induced by band-folding from the moiré superlattice potential for engineering topological minibands in moiré materials. We illustrate this mechanism via two classes of model Hamiltonians, namely the Rashba model and the Bernevig-Hughes-Zhang (BHZ) model, under the moiré superlattice potentials. Moiré minibands with non-trivial band topology, including \mathbb{Z}_2 number, mirror Chern number and fragile topology, have been found and the topological phase diagram is constructed for these moiré models. A general theory based on band representations in the moiré Brillouin zone is also developed for a generalization of this mechanism to other space groups. Possible experimental realizations of our model Hamiltonian are discussed.

Introduction - Recent experimental realizations of topologically non-trivial flat bands in moiré materials, including twisted bilayer graphene[1–12], multilayer rhombohedral graphene/hexagonal boron nitride moiré heterostructures[13–17], twisted monolayer-bilayer graphene[18, 19], and transition metal dichalcogenides moiré superlattice[20–27], have led to the successful discovery of a variety of integer and fractional Chern insulator phases. Topologically non-trivial flat bands in the existing moiré materials all originate from the K point in the atomic Brillouin zone (ABZ), presumably because the effective model around the K point does not respect time reversal \mathcal{T} so that non-trivial Berry curvature can occur locally around K while the whole system still preserves \mathcal{T} . The Coulomb interaction, combined with the local Berry curvature around K , can together produce ferromagnetic states that spontaneously break \mathcal{T} and lead to the quantum anomalous Hall state [28, 29] at integer filling per moiré Brillouin zone (MBZ), and the fractional Chern insulator phase at fractional filling. In contrast, Γ ($\mathbf{k} = 0$) is a \mathcal{T} -invariant momentum in the ABZ and Kramers' theorem guarantees a spin degeneracy at Γ . The Kramers' pair of bands generally have opposite Berry curvature, so moiré flat bands originating from Γ are usually found to be topologically trivial in \mathcal{T} -invariant materials [30–32]. Breaking \mathcal{T} explicitly via external magnetic fields or magnetic materials has been theoretically proposed to achieve topological flat bands around Γ [33, 34].

In this work, we introduce a band-folding induced band inversion mechanism to realize topologically non-trivial flat bands around Γ in the ABZ for \mathcal{T} -invariant systems under moiré superlattice potentials, based on two classes of models, namely the Rashba model[35] and Bernevig-Hughes-Zhang (BHZ) model[36]. The key feature in both

classes of models is that the band minimum or maximum is slightly away from Γ in the ABZ. When the moiré length scale introduced by the moiré superlattice potential is comparable to the length scale related to the band minimum or maximum, the band folding from the higher MBZs into the 1st MBZ can lead to a band inversion, thus giving rise to topologically nontrivial flat minibands.

The general scenario of the band-folding induced band inversion mechanism for the moiré Rashba model is schematically illustrated in Fig. 1, where the topological property of the lowest energy moiré miniband is controlled by two length scales: the length scale L_R of Rashba spin-orbit-coupling (SOC) that characterizes spin precession[37] and the moiré length L_M , as shown in Fig. 1(a). For a weak Rashba SOC with $L_R \gg L_M$, the band minima are located at $\pi/2L_R$ lies in the 1st MBZ (the green region in Fig. 1(b)) and the lowest energy miniband comes from the 1st MBZ in Fig. 1(c). When increasing Rashba SOC up to $L_R \sim L_M$, the band minima move to the boundary between the 1st MBZ and the 2nd MBZ (the orange region in Fig. 1(b)), so that the minibands folded from the 2nd MBZ move down in energy, as shown in Fig. 1(d), and can eventually be lower in energy than the minibands from the 1st MBZ when $L_R \ll L_M$, as shown in Fig. 1(e). A band inversion between the minibands from the 1st and 2nd MBZs occurs and leads to the emergence of topologically non-trivial minibands. As the Rashba SOC can be tuned via external electric gates, one can electrically engineer band topology in moiré Rashba materials.

The above scenario can also be applied to the BHZ model which is applicable to a class of semiconductor quantum wells (QWs), e.g. HgTe/CdTe QWs[36] and InAs/GaSb QWs[38]. The valence band maximum in these QWs can be away from Γ , so that the band-folding induced by a moiré superlattice potential can give rise to topological valence minibands (Fig. 3a). We study the topological phase diagram of the highest valence miniband and identify the parameter regimes for topological

* These authors contributed equally.

† Corresponding author.

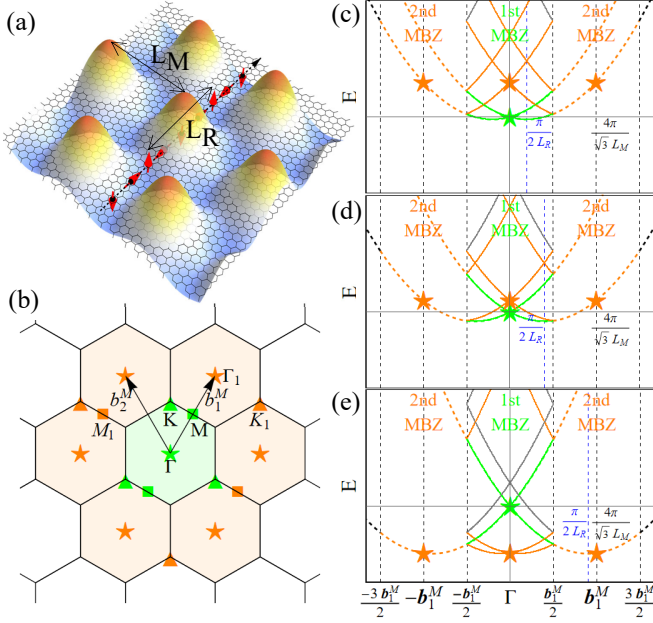


FIG. 1. (a) Schematic figure for moiré Rashba systems. An electron on the atomic lattice (black) moves under the moiré potential along the black dashed line. Red arrows are electron spins. L_R is the spin precession length. L_M is the moiré unit cell length. (b) Extended MBZ with high symmetry points. Green points Γ, M, K are located at the green 1st MBZ. Orange points Γ_1, M_1, K_1 are located at the orange 2nd MBZ. (c) - (e) Schematic moiré Rashba spectra with increasing Rashba SOC strength or moiré unit cell length. The orange dashed lines are unfolded spectra lying in the 2nd MBZ. The green, orange, and gray solid lines are moiré minibands folded from the 1st, 2nd and higher MBZ, respectively. The green (orange) star labels the state at Γ (\mathbf{b}_1^M).

phases with different mirror Chern numbers and fragile topology. A general formalism based on topological quantum chemistry (TQC) [39–41] is developed to analyze topological moiré minibands for a general space group, which demonstrates that our band-folding mechanism can serve as an efficient approach to induce non-trivial band topology in a class of moiré materials.

Moiré Rashba systems - Our first example to illustrate this mechanism is the moiré Rashba system, which is schematically shown in Fig. 1(a) with the model Hamiltonian $H = H_R + H_M$, where H_R is the Rashba model Hamiltonian

$$H_R(\mathbf{k}) = ak^2\sigma_0 + \lambda(k_y\sigma_x - k_x\sigma_y) \quad (1)$$

where σ_0 is identity matrix, $\sigma_{x,y,z}$ are Pauli matrices for spin operators, $a > 0$ is the parameter characterizing the effective mass, and $\lambda > 0$ is the Rashba SOC strength that induces spin precession with the length $L_R = \pi a/\lambda$. We consider a hexagonal moiré superlattice potential

$$H_M(\mathbf{r}) = \Delta_1 \sum_{\mathbf{g}} e^{i\mathbf{g}\cdot\mathbf{r}} \sigma_0, \quad (2)$$

where \mathbf{g} labels the moiré reciprocal lattice vectors and Δ_1

denotes the moiré potential strength. We consider \mathbf{g} up to the first shell in the MBZ, $\mathbf{g} = \pm\mathbf{b}_1^M, \pm\mathbf{b}_2^M, \pm(\mathbf{b}_1^M - \mathbf{b}_2^M)$, as marked by orange stars in Fig. 1(b), where $\mathbf{b}_1^M = 4\pi/\sqrt{3}L_M(1/2, \sqrt{3}/2)$, $\mathbf{b}_2^M = 4\pi/\sqrt{3}L_M(-1/2, \sqrt{3}/2)$ are the primitive moiré reciprocal lattice vectors and L_M is the moiré unit cell length. $E_0 = a|\mathbf{b}_1^M|^2$ sets the energy unit. We consider the space group $P6mm$ that corresponds to the point group C_{6v} [42] for moiré Rashba materials. To analyze band topology of this model using TQC [39–41], we need to identify the possible irreducible representations (irreps) of the minibands at all high symmetry momenta, including Γ, M and K , in the MBZ. The wave vector groups $G_{\mathbf{k}}$ and the double group irreps at these momenta are listed in Fig. 2b. We find the low-energy moiré minibands can be characterized by $\bar{\Gamma}_7, \bar{\Gamma}_8, \bar{\Gamma}_9$ at Γ , which are all 2D irreps due to \mathcal{T} , two 1D irreps \bar{K}_4, \bar{K}_5 and one 2D irrep \bar{K}_6 at K , and only one 2D irrep \bar{M}_5 at M . More details about the irreps are shown in the character tables in SM Sec. II A.

Tuning the Rashba parameter λ and moiré length L_M to move the Rashba band minima across the MBZ boundary can lead to non-trivial bulk topology via the band folding mechanism. The topological phase diagram of the lowest energy minibands, denoted as CB1, as a function of $\sqrt{3}L_M/4L_R$ and Δ_1/E_0 is shown in Fig. 2a. When $L_R \gg \sqrt{3}L_M/4$, the CB1 has a band touching with higher energy minibands, so it is in the semimetal phase. When $L_R \sim \sqrt{3}L_M/8 < L_M\sqrt{3}/4$, we find a blue region in which the CB1 carries nontrivial \mathbb{Z}_2 topology. Fig. 2c-f show the energy spectrum of minibands for the parameters corresponding to the points c-f in Fig. 2a, and illustrate the occurrence of a band inversion through the exchange of irreps at high symmetry points Γ, K . Fig. 2c depicts the energy dispersion of minibands for $\sqrt{3}L_M/4L_R = 0.1$ and $\Delta_1 = 0$ (the point c in Fig. 2a), where the states of CB1 at Γ, K, M all come from the 1st MBZ shown by the green markers in Fig. 1b. Fig. 2d shows the energy dispersion for the same $\sqrt{3}L_M/4L_R$ but a non-zero moiré potential $\Delta_1 = 0.1E_0$. Two spin degenerate states of CB1 at Γ belong to the $\bar{\Gamma}_9$ irrep, represented by black dots illustrated in Fig. 2b. At K , two spin states of CB1 are split. The lower energy state of CB1 belongs to the 1D irrep \bar{K}_5 while the higher energy state of CB1 belongs to the 2D irrep \bar{K}_6 and is degenerate with another higher energy miniband of CB2, resulting in a semimetal phase for point d in Fig. 2a. In Fig. 2e with $\sqrt{3}L_M/4L_R = 1.9$ and $\Delta_1 = 0$, the CB1 at Γ, M and K are all from the 2nd MBZ, as shown by the orange markers in Fig. 1b. Increasing the moiré potential to $\Delta_1 = 0.1E_0$, we notice that the irreps of CB1 at Γ and K belong to $\bar{\Gamma}_8$ and \bar{K}_6 , respectively, both of which are 2D irreps (SM Sec. II A). Thus, CB1 are separated from CB2 by a mini-gap and become isolated moiré minibands. The Wannier center flow [43] in the insets of Fig. 2f demonstrates nontrivial \mathbb{Z}_2 topology of CB1. In Fig. 2a, the dashed line around $L_R \sim L_M\sqrt{3}/4$ labels the interchange of $\bar{\Gamma}_9$ from the 1st MBZ and $\bar{\Gamma}_8$ from the 2nd MBZ for CB1 at Γ , while the solid line that separates white and blue regions represents

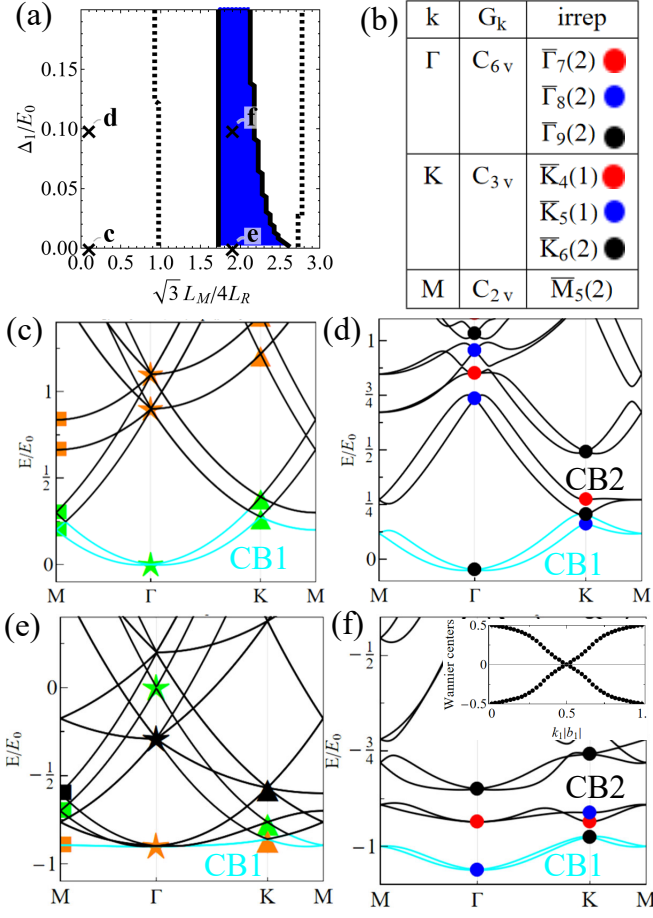


FIG. 2. (a) Topological phase diagram of the lowest-energy conduction band CB1. Blue regions are topological insulator phases with nontrivial \mathbb{Z}_2 . White regions are semi-metal phases. (b) High symmetry points Γ, M, K , wavevector group G_k , and symmetry irreps with dimensions in the parentheses. Colored dots represent irreps in spectra (d)(f). Black dashed lines in (a) denote the exchange of irreps $\bar{\Gamma}_8$ and $\bar{\Gamma}_9$. Black solid lines denote the exchange of symmetry irreps at K between \bar{K}_6 and \bar{K}_4 , or between \bar{K}_6 and \bar{K}_5 . (c)-(f) spectra with parameters at points c-f in (a), respectively. Colored dots in (c)(e) represent states at extended MBZ points in 1(b). Green (orange) color represents the 1st (2nd) MBZ. Insets in (f) show Wannier center flow for CB1.

the interchange of the \bar{K}_6 and \bar{K}_5 minibands at K . The interchange between the minibands from different MBZs is the origin of non-trivial topology for CB1.

Moiré BHZ systems - Our second example is the BHZ model that has been successfully applied to HgTe QWs [44], in which the early literature has revealed the valence band maximum away from Γ in the inverted band regime [45, 46]. The Hamiltonian of the BHZ model is described in SM Sec.III.A, and the key parameter is the gap parameter, denoted as m in Fig. 3a, which controls the normal or inverted band structure, depending on its sign. Fig. 3a shows the schematic unfolded band spectrum of the BHZ model with the valence band maxima

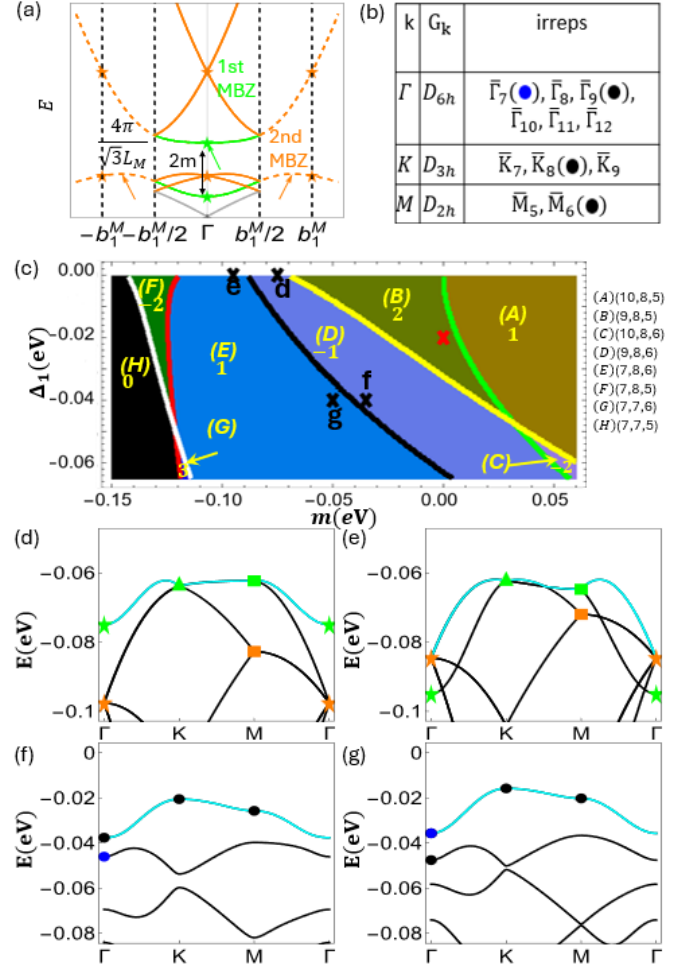


FIG. 3. (a) Schematic band folding in the moiré BHZ system. The orange dashed lines are unfolded spectra lying in the 2nd MBZ. The green (orange) solid lines are moiré minibands folded from the 1st (2nd) MBZ. The gray solid lines are minibands from higher MBZ. The green (orange) star labels the state at Γ ($|b_1^M\rangle$). $2m$ labels the gap at Γ . The orange arrow points to the maximum of the valence band. (b) Wavevector group G_k of high symmetry points Γ, M, K for space group $p6/mmm$. All symmetry irreps are 2D. Colored dots are representation of irreps in spectra in (f) and (g). (c) Topological phase diagram of VB1. Different color regions (A)-(H) distinguish irreps at high symmetry points, labeled by (i, j, k) , which is short for $(\bar{\Gamma}_i, \bar{K}_j, \bar{M}_k)$ of VB1. The number shows the mirror Chern number C_M . The colored solid lines between different regions identify irreps interchanges at high symmetry points. Band dispersion for the parameters labeled by the red cross is shown in the Fig. 4a. (d)-(g) Band dispersion with the parameters labeled by the black crosses d-g in (c). The VB1 is highlighted by cyan.

located around $k_{max} \sim \sqrt{|m/B|}$ away from Γ , where B is the coefficient of k^2 term in the BHZ model, as depicted by the orange arrow in Fig. 3a, which can be achieved for a negative m (SM Sec.III.A). The moiré potential has the same form as Eq. (2) with the potential strength Δ_1 . When the moiré reciprocal lattice vector

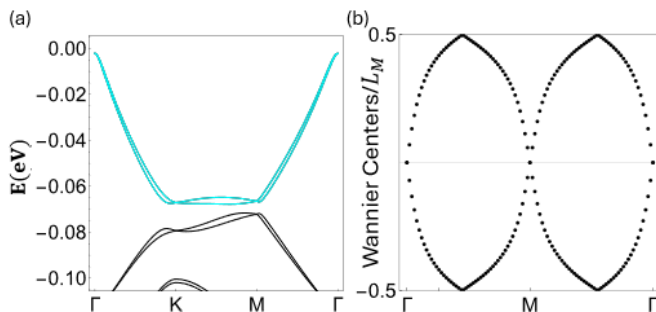


FIG. 4. (a) Band dispersion with Rashba SOC strength $\lambda=0.02$ nm·eV and parameters labeled by the red cross in Fig. 3c. (b) Wannier center flow for VB1. The Wannier center flow still reveals a double winding feature when Rashba SOC is included.

$|\mathbf{b}_1^M|$ is comparable to the valence band maxima k_{max} , we expect the band inversion due to band-folding can occur. We consider the space group for the moiré BHZ system to be $P6/mmm$ corresponding to the point group D_{6h} [42]. Due to the combined symmetry of \mathcal{T} and inversion \mathcal{I} , all irreps are 2D so that all minibands are doubly degenerate for spin, which facilitates the existence of isolated minibands, in sharp contrast with spin-split bands in the Rashba model due to the absence of inversion \mathcal{I} . At inversion-symmetric momenta Γ and M , mini-bands can be characterized by $\bar{\Gamma}_7, \bar{\Gamma}_8, \bar{\Gamma}_9$ and \bar{M}_5 with even parities under \mathcal{I} , and $\bar{\Gamma}_{10}, \bar{\Gamma}_{11}, \bar{\Gamma}_{12}$ and \bar{M}_6 with odd parities. At K , three 2D irreps $\bar{K}_7, \bar{K}_8, \bar{K}_9$ can appear for minibands. All these symmetry properties of minibands are summarized in Fig. 3b.

Due to higher symmetry and non-trivial band topology in the unfolded BHZ model, a rich topological phase diagram emerges for the moiré BHZ model, as compared to the moiré Rashba model. Here we focus on the top valence minibands, denoted as VB1, in the negative Δ_1 regime, in which the VB1 feels a moiré potential of honeycomb lattice. Due to the existence of the out-of-plane mirror symmetry \mathcal{M}_z [47, 48], the topological phase diagram can be characterized by the mirror Chern number C_M . The mirror Chern number C_M and the irreps at high symmetry momenta (Γ, K, M) for the VB1 as a function of m and Δ_1 are summarized in Fig. 3c, in which multiple topological phase transition lines are found and have different physical origins. For a positive m and a small value of $|\Delta_1|$, the valence band maximum of the unfolded BHZ model is at Γ and thus the phase transitions for VB1 (green and yellow lines in Fig. 3c) only involve the states within the 1st MBZ. The green transition line between the phases A and B corresponds to the band inversion of the unfolded BHZ model at Γ and changes C_M by 1, while the yellow transition line between the phases B (A) and D (C) corresponds to the band inversion at three equivalent M at the boundary of the 1st MBZ and thus changes C_M by 3 (SM Sec.III.B). Further reducing m towards the black transition line in Fig. 3c, the valence band maximum moves towards the

2nd MBZ, as depicted in Fig. 3d and e at $\Delta_1 = 0$, and the band-folding mechanism starts working. Across the black transition line, the energy of the $\bar{\Gamma}_7$ state at Γ in the 2nd MBZ becomes lower than that of the $\bar{\Gamma}_9$ state in the 1st MBZ, so a band inversion occurs for the VB1 due to the exchange of the $\bar{\Gamma}_9$ and $\bar{\Gamma}_7$ irrep states, as shown in Fig. 3f and g. We also find that this transition has the form of a quadratic band touching at the transition point (SM Sec.III.B) and changes C_M by 2. Consequently, the C_M of VB1 changes from $C_M = -1$ in region D to $C_M = 1$ in region E (Fig. 3f and g). With further reducing m , the red transition line is for the band inversion for the minibands at M of the 2nd MBZ, which varies C_M by 3, while the white line is for the transition of the minibands at K in the 2nd MBZ that have lower energy than those at K in the 1st MBZ. As there are two different K s in the MBZ, the mirror Chern number of VB1 changes by 2 across the white line, and we find $C_M = -2$ in region F and $C_M = 0$ in region H.

We next point out unique aspects of the minibands for the moiré BHZ model, which are absent for the moiré Rashba model. We first notice the VB1 with $C_M = \pm 2$ in the B, C and F regions. These phases possess two copies of helical edge modes at the boundary. Previous theoretical studies [49–51] proposed strong interactions in the $C_M = \pm 2$ phase can give rise to a bosonic symmetry protected topological phase, which is characterized by a bosonic mode at the boundary instead of a fermionic mode. When mirror symmetry is broken by applying an out-of-plane electric field via gate voltages [52], C_M loses its physical meaning and the corresponding helical edge modes are expected to gap out. The band dispersion and Wannier center flow in this case are shown in 4a and b as an example, respectively. Strikingly, the Wannier center flow of VB1 shown in 4b still has a winding number $w = 2$, independent of mirror symmetry breaking. This nontrivial double winding of Wannier centers indicate fragile topology [53–59], protected by $C_{2z}\mathcal{T}$, where C_{2z} is the two-fold rotation symmetry. The nature of fragile topology can be revealed by including additional trivial bands to gap out the double winding of Wannier centers, as discussed SM Sec.III.C. In addition, the topologically nontrivial minibands in region E are relatively flat with its miniband width smaller than 2.5 meV and minigap around 20 meV, potentially supporting a fractional Chern insulator phase, which was very recently discussed in Ref.[60].

Conclusion and discussion - In conclusion, the band-folding mechanism can give rise to band inversion of moiré minibands in different extended MBZs and induces nontrivial \mathbb{Z}_2 topology, fragile topology, mirror Chern topology and topological flat minibands in the Rashba and BHZ systems under moiré superlattice potentials. The band-folding mechanism for topological minibands can be generalized to other moiré materials with different space group symmetries. The SM Sec. I describes a general approach based on the TQC method[39, 42, 61] to classify the irreps of minibands by combining the group

theory analysis of band-folding mechanism with the perturbation theory in the weak moiré potential limit. Applying this method to the moiré Rashba and BHZ models is also discussed in SM Sec. II and III, respectively.

A class of semiconductor heterostructures with large Rashba SOC and high electron mobility is identified in the SM Sec.II.B for possible material realizations of moiré Rashba systems. The BHZ model can be realized by HgTe/CdTe QWs[36, 62], InAs/GaSb QWs[38, 63], and monolayer 1T'-WTe₂[64]. The superlattice potential could be created by moiré 2D insulating materials, such as boron nitride or transition metal dichalcogenides[65–70], or by the patterned hole array in dielectric substrate materials to form a superlattice potential[71, 72].

The great tunability of moiré structure and the potential strong Coulomb interaction of moiré minibands may allow us to realize bosonic SPT phase [49, 51] and $\mathcal{C}_{2z}\mathcal{T}$ -protected $w = 2$ fragile topology [73], which have not been realized in atomic crystals so far.

Acknowledgement - We thank Liang Fu, Jainendra K Jain, Zhen Bi, Jiabin Yu, Lujin Min, Ke Huang for helpful discussion. K.J.Y., Y.Z.L. and C.X.L. acknowledge the support from the NSF through The Pennsylvania State University Materials Research Science and Engineering Center [DMR-2011839]. C.-X.L. also acknowledge support from NSF grant via the grant number DMR-2241327 and also the grant NSF PHY-1748958 to the Kavli Institute for Theoretical Physics (KITP).

-
- [1] R. Bistritzer and A. H. MacDonald, Moiré bands in twisted double-layer graphene, *Proceedings of the National Academy of Sciences* **108**, 12233 (2011).
- [2] A. L. Sharpe, E. J. Fox, A. W. Barnard, J. Finney, K. Watanabe, T. Taniguchi, M. Kastner, and D. Goldhaber-Gordon, Emergent ferromagnetism near three-quarters filling in twisted bilayer graphene, *Science* **365**, 605 (2019).
- [3] M. Serlin, C. Tschirhart, H. Polshyn, Y. Zhang, J. Zhu, K. Watanabe, T. Taniguchi, L. Balents, and A. Young, Intrinsic quantized anomalous hall effect in a moiré heterostructure, *Science* **367**, 900 (2020).
- [4] Y.-H. Zhang, D. Mao, and T. Senthil, Twisted bilayer graphene aligned with hexagonal boron nitride: Anomalous hall effect and a lattice model, *Physical Review Research* **1**, 033126 (2019).
- [5] N. Bultinck, S. Chatterjee, and M. P. Zaletel, Mechanism for anomalous hall ferromagnetism in twisted bilayer graphene, *Physical review letters* **124**, 166601 (2020).
- [6] M. Xie and A. H. MacDonald, Nature of the correlated insulator states in twisted bilayer graphene, *Physical review letters* **124**, 097601 (2020).
- [7] Y. Xie, A. T. Pierce, J. M. Park, D. E. Parker, E. Khalaf, P. Ledwith, Y. Cao, S. H. Lee, S. Chen, P. R. Forrester, *et al.*, Fractional chern insulators in magic-angle twisted bilayer graphene, *Nature* **600**, 439 (2021).
- [8] E. M. Spanton, A. A. Zibrov, H. Zhou, T. Taniguchi, K. Watanabe, M. P. Zaletel, and A. F. Young, Observation of fractional chern insulators in a van der waals heterostructure, *Science* **360**, 62 (2018).
- [9] P. J. Ledwith, G. Tarnopolsky, E. Khalaf, and A. Vishwanath, Fractional chern insulator states in twisted bilayer graphene: An analytical approach, *Physical Review Research* **2**, 023237 (2020).
- [10] A. Abouelkomsan, Z. Liu, and E. J. Bergholtz, Particle-hole duality, emergent fermi liquids, and fractional chern insulators in moiré flatbands, *Physical review letters* **124**, 106803 (2020).
- [11] C. Repellin and T. Senthil, Chern bands of twisted bilayer graphene: Fractional chern insulators and spin phase transition, *Physical Review Research* **2**, 023238 (2020).
- [12] P. Wilhelm, T. C. Lang, and A. M. Läuchli, Interplay of fractional chern insulator and charge density wave phases in twisted bilayer graphene, *Physical Review B* **103**, 125406 (2021).
- [13] G. Chen, A. L. Sharpe, E. J. Fox, Y.-H. Zhang, S. Wang, L. Jiang, B. Lyu, H. Li, K. Watanabe, T. Taniguchi, *et al.*, Tunable correlated chern insulator and ferromagnetism in a moiré superlattice, *Nature* **579**, 56 (2020).
- [14] Z. Lu, T. Han, Y. Yao, A. P. Reddy, J. Yang, J. Seo, K. Watanabe, T. Taniguchi, L. Fu, and L. Ju, Fractional quantum anomalous hall effect in multilayer graphene, *Nature* **626**, 759 (2024).
- [15] G. Chen, L. Jiang, S. Wu, B. Lyu, H. Li, B. L. Chittari, K. Watanabe, T. Taniguchi, Z. Shi, J. Jung, *et al.*, Evidence of a gate-tunable mott insulator in a trilayer graphene moiré superlattice, *Nature Physics* **15**, 237 (2019).
- [16] B. L. Chittari, G. Chen, Y. Zhang, F. Wang, and J. Jung, Gate-tunable topological flat bands in trilayer graphene boron-nitride moiré superlattices, *Physical review letters* **122**, 016401 (2019).
- [17] Y.-H. Zhang, D. Mao, Y. Cao, P. Jarillo-Herrero, and T. Senthil, Nearly flat chern bands in moiré superlattices, *Physical Review B* **99**, 075127 (2019).
- [18] H. Polshyn, J. Zhu, M. A. Kumar, Y. Zhang, F. Yang, C. L. Tschirhart, M. Serlin, K. Watanabe, T. Taniguchi, A. H. MacDonald, *et al.*, Electrical switching of magnetic order in an orbital chern insulator, *Nature* **588**, 66 (2020).
- [19] S. Chen, M. He, Y.-H. Zhang, V. Hsieh, Z. Fei, K. Watanabe, T. Taniguchi, D. H. Cobden, X. Xu, C. R. Dean, *et al.*, Electrically tunable correlated and topological states in twisted monolayer-bilayer graphene, *Nature Physics* **17**, 374 (2021).
- [20] T. Li, S. Jiang, B. Shen, Y. Zhang, L. Li, Z. Tao, T. Devakul, K. Watanabe, T. Taniguchi, L. Fu, *et al.*, Quantum anomalous hall effect from intertwined moiré bands, *Nature* **600**, 641 (2021).
- [21] J. Cai, E. Anderson, C. Wang, X. Zhang, X. Liu, W. Holtzmann, Y. Zhang, F. Fan, T. Taniguchi, K. Watanabe, *et al.*, Signatures of fractional quantum anomalous hall states in twisted mote2, *Nature* **622**, 63 (2023).
- [22] H. Park, J. Cai, E. Anderson, Y. Zhang, J. Zhu, X. Liu, C. Wang, W. Holtzmann, C. Hu, Z. Liu, *et al.*, Observation of fractionally quantized anomalous hall effect, Na-

- ture **622**, 74 (2023).
- [23] Y. Zeng, Z. Xia, K. Kang, J. Zhu, P. Knüppel, C. Vaswani, K. Watanabe, T. Taniguchi, K. F. Mak, and J. Shan, Thermodynamic evidence of fractional chern insulator in moiré mote2, *Nature* **622**, 69 (2023).
- [24] F. Xu, Z. Sun, T. Jia, C. Liu, C. Xu, C. Li, Y. Gu, K. Watanabe, T. Taniguchi, B. Tong, *et al.*, Observation of integer and fractional quantum anomalous hall effects in twisted bilayer mote 2, *Physical Review X* **13**, 031037 (2023).
- [25] F. Wu, T. Lovorn, E. Tutuc, I. Martin, and A. MacDonald, Topological insulators in twisted transition metal dichalcogenide homobilayers, *Physical review letters* **122**, 086402 (2019).
- [26] H. Li, U. Kumar, K. Sun, and S.-Z. Lin, Spontaneous fractional chern insulators in transition metal dichalcogenide moiré superlattices, *Physical Review Research* **3**, L032070 (2021).
- [27] T. Devakul, V. Crépel, Y. Zhang, and L. Fu, Magic in twisted transition metal dichalcogenide bilayers, *Nature communications* **12**, 6730 (2021).
- [28] C.-Z. Chang, J. Zhang, X. Feng, J. Shen, Z. Zhang, M. Guo, K. Li, Y. Ou, P. Wei, L.-L. Wang, *et al.*, Experimental observation of the quantum anomalous hall effect in a magnetic topological insulator, *Science* **340**, 167 (2013).
- [29] C.-Z. Chang, C.-X. Liu, and A. H. MacDonald, Colloquium: Quantum anomalous hall effect, *Reviews of Modern Physics* **95**, 011002 (2023).
- [30] B. A. Foutty, J. Yu, T. Devakul, C. R. Kometter, Y. Zhang, K. Watanabe, T. Taniguchi, L. Fu, and B. E. Feldman, Tunable spin and valley excitations of correlated insulators in γ -valley moiré bands, *Nature Materials* **22**, 731 (2023).
- [31] L. Xian, M. Claassen, D. Kiese, M. M. Scherer, S. Trebst, D. M. Kennes, and A. Rubio, Realization of nearly dispersionless bands with strong orbital anisotropy from destructive interference in twisted bilayer mos2, *Nature communications* **12**, 5644 (2021).
- [32] M. Angeli and A. H. MacDonald, γ valley transition metal dichalcogenide moiré bands, *Proceedings of the National Academy of Sciences* **118**, e2021826118 (2021).
- [33] J. Dong, J. Wang, and L. Fu, Dirac electron under periodic magnetic field: Platform for fractional chern insulator and generalized wigner crystal, *arXiv preprint arXiv:2208.10516* (2022).
- [34] N. Paul, Y. Zhang, and L. Fu, Giant proximity exchange and flat chern band in 2d magnet-semiconductor heterostructures, *Science Advances* **9**, eabn1401 (2023).
- [35] Y. A. Bychkov and E. I. Rashba, Oscillatory effects and the magnetic susceptibility of carriers in inversion layers, *Journal of physics C: Solid state physics* **17**, 6039 (1984).
- [36] B. A. Bernevig, T. L. Hughes, and S.-C. Zhang, Quantum spin hall effect and topological phase transition in hgte quantum wells, *science* **314**, 1757 (2006).
- [37] S. Datta and B. Das, Electronic analog of the electrooptic modulator, *Applied Physics Letters* **56**, 665 (1990).
- [38] C. Liu, T. L. Hughes, X.-L. Qi, K. Wang, and S.-C. Zhang, Quantum spin hall effect in inverted type-ii semiconductors, *Physical review letters* **100**, 236601 (2008).
- [39] B. Bradlyn, L. Elcoro, J. Cano, M. G. Vergniory, Z. Wang, C. Felser, M. I. Aroyo, and B. A. Bernevig, Topological quantum chemistry, *Nature* **547**, 298 (2017).
- [40] J. Cano and B. Bradlyn, Band representations and topological quantum chemistry, *Annual Review of Condensed Matter Physics* **12**, 225 (2021).
- [41] L. Elcoro, B. J. Wieder, Z. Song, Y. Xu, B. Bradlyn, and B. A. Bernevig, Magnetic topological quantum chemistry, *Nature communications* **12**, 5965 (2021).
- [42] L. Elcoro, B. Bradlyn, Z. Wang, M. G. Vergniory, J. Cano, C. Felser, B. A. Bernevig, D. Orobengoa, G. Flor, and M. I. Aroyo, Double crystallographic groups and their representations on the bilbao crystallographic server, *Journal of Applied Crystallography* **50**, 1457 (2017).
- [43] R. Yu, X. L. Qi, A. Bernevig, Z. Fang, and X. Dai, Equivalent expression of z2 topological invariant for band insulators using the non-abelian berry connection, *Physical Review B* **84**, 075119 (2011).
- [44] D. Rothe, R. Reinthaler, C. Liu, L. Molenkamp, S. Zhang, and E. Hankiewicz, Fingerprint of different spin-orbit terms for spin transport in hgte quantum wells, *New Journal of Physics* **12**, 065012 (2010).
- [45] K. Ortner, X. Zhang, A. Pfeuffer-Jeschke, C. Becker, G. Landwehr, and L. Molenkamp, Valence band structure of hgte/hg 1- x cd x te single quantum wells, *Physical Review B* **66**, 075322 (2002).
- [46] E. Novik, A. Pfeuffer-Jeschke, T. Jungwirth, V. Latussek, C. Becker, G. Landwehr, H. Buhmann, and L. Molenkamp, Band structure of semimagnetic hg 1- y mn y te quantum wells, *Physical Review B* **72**, 035321 (2005).
- [47] J. C. Teo, L. Fu, and C. Kane, Surface states and topological invariants in three-dimensional topological insulators: Application to bi 1- x sb x, *Physical Review B* **78**, 045426 (2008).
- [48] Y. Ando and L. Fu, Topological crystalline insulators and topological superconductors: From concepts to materials, *Annu. Rev. Condens. Matter Phys.* **6**, 361 (2015).
- [49] Z. Bi, R. Zhang, Y.-Z. You, A. Young, L. Balents, C.-X. Liu, and C. Xu, Bilayer graphene as a platform for bosonic symmetry-protected topological states, *Physical review letters* **118**, 126801 (2017).
- [50] R.-X. Zhang and C.-X. Liu, Fingerprints of a bosonic symmetry-protected topological state in a quantum point contact, *Physical review letters* **118**, 216803 (2017).
- [51] R.-X. Zhang, C. Xu, and C.-X. Liu, Interacting topological phases in thin films of topological mirror kondo insulators, *Physical Review B* **94**, 235128 (2016).
- [52] R. Winkler, Spin-orbit coupling effects in two-dimensional electron and hole systems, *Springer Tracts in Modern Physics*, Berlin: Springer **191** (2003).
- [53] H. C. Po, H. Watanabe, and A. Vishwanath, Fragile topology and wannier obstructions, *Physical review letters* **121**, 126402 (2018).
- [54] A. Alexandradinata, X. Dai, and B. A. Bernevig, Wilson-loop characterization of inversion-symmetric topological insulators, *Physical Review B* **89**, 155114 (2014).
- [55] B. Bradlyn, Z. Wang, J. Cano, and B. A. Bernevig, Disconnected elementary band representations, fragile topology, and wilson loops as topological indices: An example on the triangular lattice, *Physical Review B* **99**, 045140 (2019).
- [56] J. Cano, B. Bradlyn, Z. Wang, L. Elcoro, M. Vergniory, C. Felser, M. Aroyo, and B. A. Bernevig, Topology of disconnected elementary band representations, *Physical review letters* **120**, 266401 (2018).

- [57] B. J. Wieder and B. A. Bernevig, The axion insulator as a pump of fragile topology, arXiv preprint arXiv:1810.02373 (2018).
- [58] A. Bouhon, A. M. Black-Schaffer, and R.-J. Slager, Wilson loop approach to fragile topology of split elementary band representations and topological crystalline insulators with time-reversal symmetry, *Physical Review B* **100**, 195135 (2019).
- [59] B. J. Wieder, Z. Wang, J. Cano, X. Dai, L. M. Schoop, B. Bradlyn, and B. A. Bernevig, Strong and fragile topological dirac semimetals with higher-order fermi arcs, *Nature communications* **11**, 627 (2020).
- [60] T. Tan, A. P. Reddy, L. Fu, and T. Devakul, Designing topology and fractionalization in narrow gap semiconductor films via electrostatic engineering, arXiv preprint arXiv:2402.03085 (2024).
- [61] M. Vergniory, L. Elcoro, Z. Wang, J. Cano, C. Felser, M. Aroyo, B. A. Bernevig, and B. Bradlyn, Graph theory data for topological quantum chemistry, *Physical Review E* **96**, 023310 (2017).
- [62] M. König, S. Wiedmann, C. Brune, A. Roth, H. Buhmann, L. W. Molenkamp, X.-L. Qi, and S.-C. Zhang, Quantum spin hall insulator state in hgte quantum wells, *Science* **318**, 766 (2007).
- [63] L. Du, I. Knez, G. Sullivan, and R.-R. Du, Robust helical edge transport in gated inas/gasb bilayers, *Physical review letters* **114**, 096802 (2015).
- [64] S. Tang, C. Zhang, D. Wong, Z. Pedramrazi, H.-Z. Tsai, C. Jia, B. Moritz, M. Claassen, H. Ryu, S. Kahn, *et al.*, Quantum spin hall state in monolayer 1t'-wte2, *Nature Physics* **13**, 683 (2017).
- [65] K. Yasuda, X. Wang, K. Watanabe, T. Taniguchi, and P. Jarillo-Herrero, Stacking-engineered ferroelectricity in bilayer boron nitride, *Science* **372**, 1458 (2021).
- [66] P. Zhao, C. Xiao, and W. Yao, Universal superlattice potential for 2d materials from twisted interface inside h-bn substrate, *npj 2D Materials and Applications* **5**, 38 (2021).
- [67] D. S. Kim, R. C. Dominguez, R. Mayorga-Luna, D. Ye, J. Embley, T. Tan, Y. Ni, Z. Liu, M. Ford, F. Y. Gao, *et al.*, Electrostatic moiré potential from twisted hexagonal boron nitride layers, *Nature materials* **23**, 65 (2024).
- [68] C. Woods, P. Ares, H. Nevison-Andrews, M. Holwill, R. Fabregas, F. Guinea, A. Geim, K. Novoselov, N. Walet, and L. Fumagalli, Charge-polarized interfacial superlattices in marginally twisted hexagonal boron nitride, *Nature communications* **12**, 347 (2021).
- [69] X. Wang, K. Yasuda, Y. Zhang, S. Liu, K. Watanabe, T. Taniguchi, J. Hone, L. Fu, and P. Jarillo-Herrero, Interfacial ferroelectricity in rhombohedral-stacked bilayer transition metal dichalcogenides, *Nature nanotechnology* **17**, 367 (2022).
- [70] Y. Xu, C. Horn, J. Zhu, Y. Tang, L. Ma, L. Li, S. Liu, K. Watanabe, T. Taniguchi, J. C. Hone, *et al.*, Creation of moiré bands in a monolayer semiconductor by spatially periodic dielectric screening, *Nature Materials* **20**, 645 (2021).
- [71] C. Forsythe, X. Zhou, K. Watanabe, T. Taniguchi, A. P. Pasupathy, P. Moon, M. Koshino, P. Kim, and C. R. Dean, Band structure engineering of 2d materials using patterned dielectric superlattices, *Nature nanotechnology* **13**, 566 (2018).
- [72] D. Barcons Ruiz, H. Herzig Sheinfux, R. Hoffmann, I. Torre, H. Agarwal, R. K. Kumar, L. Vistoli, T. Taniguchi, K. Watanabe, A. Bachtold, *et al.*, Engineering high quality graphene superlattices via ion milled ultra-thin etching masks, *Nature Communications* **13**, 6926 (2022).
- [73] F. Schindler, M. Brzezińska, W. A. Benalcazar, M. Iraola, A. Bouhon, S. S. Tsirkin, M. G. Vergniory, and T. Neupert, Fractional corner charges in spin-orbit coupled crystals, *Physical Review Research* **1**, 033074 (2019).
- [74] M. S. Dresselhaus, G. Dresselhaus, and A. Jorio, *Group theory: application to the physics of condensed matter* (Springer Science & Business Media, 2007).
- [75] G. de la Flor, B. Souvignier, G. Madariaga, and M. I. Aroyo, Layer groups: Brillouin-zone and crystallographic databases on the bilbao crystallographic server, *Acta Crystallographica Section A: Foundations and Advances* **77**, 559 (2021).
- [76] M. I. Aroyo, D. Orobengoa, G. de la Flor, E. S. Tasci, J. M. Perez-Mato, and H. Wondratschek, Brillouin-zone database on the bilbao crystallographic server, *Acta Crystallographica Section A: Foundations and Advances* **70**, 126 (2014).
- [77] E. Tasci, G. de la Flor, D. Orobengoa, C. Capillas, J. Perez-Mato, and M. Aroyo, An introduction to the tools hosted in the bilbao crystallographic server, in *EPJ Web of Conferences*, Vol. 22 (EDP Sciences, 2012) p. 00009.
- [78] A. Balocchi, Q. Duong, P. Renucci, B. Liu, C. Fontaine, T. Amand, D. Lagarde, and X. Marie, Full electrical control of the electron spin relaxation in gaas quantum wells, *Physical review letters* **107**, 136604 (2011).
- [79] A. Chin, P. Martin, P. Ho, J. Ballingall, T.-h. Yu, and J. Mazurowski, High quality (111) b gaas, algaas, algaas/gaas modulation doped heterostructures and a gaas/ingaas/gaas quantum well, *Applied physics letters* **59**, 1899 (1991).
- [80] T. Hayakawa, K. Takahashi, M. Kondo, T. Suyama, S. Yamamoto, and T. Hijikata, Enhancement in optical transition in (111)-oriented gaas-algaas quantum well structures, *Physical review letters* **60**, 349 (1988).
- [81] D. Grundler, Large rashba splitting in inas quantum wells due to electron wave function penetration into the barrier layers, *Physical review letters* **84**, 6074 (2000).
- [82] J. Nitta, T. Akazaki, H. Takayanagi, and T. Enoki, Gate control of spin-orbit interaction in an inverted in_{0.53}ga_{0.47}as/in_{0.52}al_{0.48}as heterostructure, *Phys. Rev. Lett.* **78**, 1335 (1997).
- [83] I. Knez and R.-R. Du, Quantum spin hall effect in inverted inas/gasb quantum wells, *Frontiers of Physics* **7**, 200 (2012).
- [84] J. Luo, H. Munekata, F. Fang, and P. Stiles, Effects of inversion asymmetry on electron energy band structures in gasb/inas/gasb quantum wells, *Physical Review B* **41**, 7685 (1990).
- [85] B. Das, D. Miller, S. Datta, R. Reifenberger, W. Hong, P. Bhattacharya, J. Singh, and M. Jaffe, Evidence for spin splitting in in x ga 1- x as/in 0.52 al 0.48 as heterostructures as b → 0, *Physical Review B* **39**, 1411 (1989).
- [86] C. Nguyen, K. Ensslin, and H. Kroemer, Magnetotransport in inas/alsb quantum wells with large electron concentration modulation, *Surface science* **267**, 549 (1992).
- [87] K. Yang, Z. Xu, Y. Feng, F. Schindler, Y. Xu, Z. Bi, B. A. Bernevig, P. Tang, and C.-X. Liu, Topological minibands

and interaction driven quantum anomalous hall state in topological insulator based moiré heterostructures, *Nature communications* **15**, 2670 (2024).

- [88] C. Fang, M. J. Gilbert, and B. A. Bernevig, Bulk topological invariants in noninteracting point group symmetric insulators, *Physical Review B* **86**, 115112 (2012).
- [89] M. I. Aroyo, J. M. Perez-Mato, D. Orobengoa, E. Tasci, G. de la Flor, and A. Kirov, Crystallography online: Bilbao crystallographic server, *Bulg. Chem. Commun* **43**, 183 (2011).
- [90] M. I. Aroyo, A. Kirov, C. Capillas, J. Perez-Mato, and H. Wondratschek, Bilbao crystallographic server. ii. representations of crystallographic point groups and space groups, *Acta Crystallographica Section A: Foundations of Crystallography* **62**, 115 (2006).
- [91] M. I. Aroyo, J. M. Perez-Mato, C. Capillas, E. Kroumova, S. Ivantchev, G. Madariaga, A. Kirov, and H. Wondratschek, Bilbao crystallographic server: I. databases and crystallographic computing programs, *Zeitschrift für Kristallographie-Crystalline Materials* **221**, 15 (2006).

Supplementary Materials

In this Supplementary Material, we will first describe our general approach to identify topological property of moiré minibands based on topological quantum chemistry (TQC) method [39, 42, 61] in Sec. I. Then, we will apply this approach to moiré Rashba systems in Sec. II and moiré Bernevig-Hughes-Zhang (BHZ) model in Sec. III.

I. GENERAL FORMALISM FOR TOPOLOGICAL PROPERTIES OF MOIRÉ SYSTEMS BASED ON TOPOLOGICAL QUANTUM CHEMISTRY

In this section, we will develop a general approach to derive band representations of moiré minibands at high symmetry momenta under a weak moiré superlattice potential to analyze miniband topology based on the theoretical framework of topological quantum chemistry (TQC)[39, 42, 61]. The whole procedure can be implemented in five steps and a flow chart, using the moiré Rashba model as an example, is shown in Fig.S1.

Step 1: we define the moiré reciprocal lattice vectors in atomic Brillouin zone (ABZ) and label the shells of momenta in the ABZ that are folded into the same momentum in the 1st moiré Brillouin zone (MBZ). A tight-binding Hamiltonian or an effective Hamiltonian, $H_0(\mathbf{k})$, describes the electronic band structure of an atomic crystal with its crystal symmetry described by the space group, denoted by G^0 , and the crystal momentum \mathbf{k} defined in the ABZ of G^0 . For the effective model that is expanded around certain momentum in the ABZ, we can choose a crystal symmetry group that is compatible with the full symmetry property of the effective model. As an example, we choose the $P6mm$ group for the Rashba model and the $P6/mmm$ group for the BHZ model in this work. It should be emphasized that the same effective model can be applied to crystal materials with different space groups. At a certain momentum \mathbf{k}_0 in the ABZ, the wave vector group (*i.e.*, the little group that leaves this wave vector invariant) is denoted as $G_{\mathbf{k}_0}^0$. The moiré superlattice potential H_M can be described by a different space group, denoted as G^M , so the space group for the whole moiré system is described by the group $G = G^M \cap G^0$ that can be used to define the MBZ. We denote \mathbf{g}_0 and \mathbf{g} as the reciprocal lattice vectors for the space group G^0 and G , respectively. For any momentum \mathbf{k}_0 in the ABZ, one can always find a momentum $\tilde{\mathbf{k}}_0$ in the 1st MBZ so that \mathbf{k}_0 and $\tilde{\mathbf{k}}_0$ are connected by a moiré reciprocal lattice vector \mathbf{g} . The set of all momenta in the ABZ that are folded to the same $\tilde{\mathbf{k}}_0$ is defined as $A_{\tilde{\mathbf{k}}_0} = \{\mathbf{k}_0 | \mathbf{k}_0 = \tilde{\mathbf{k}}_0 + \mathbf{g}\}$. The wave vector group at $\tilde{\mathbf{k}}_0$ for the space group G is denoted as $G_{\tilde{\mathbf{k}}_0}$, which includes all the point group symmetry operators in G that transforms $\tilde{\mathbf{k}}_0$ into a momentum $\mathbf{k}_0 \in A_{\tilde{\mathbf{k}}_0}$.

$$G_{\tilde{\mathbf{k}}_0} = \{S | S\tilde{\mathbf{k}}_0 \in A_{\tilde{\mathbf{k}}_0} \ \& \ S \in O(3) \cap G\}, \quad (S1)$$

where $O(3)$ is the three dimensional orthogonal group. $G_{\mathbf{k}_0}^0$ and $G_{\tilde{\mathbf{k}}_0}$ can contain different symmetry operators for $\mathbf{k}_0 \in A_{\tilde{\mathbf{k}}_0}$. The point group of G is the wave vector group G_Γ , where Γ is the origin of the MBZ. Using the wave vector group $G_{\tilde{\mathbf{k}}_0}$, the momentum shell, denoted as $\tilde{A}_{\tilde{\mathbf{k}}_0}$ for any momentum $\mathbf{k}_0 \in A_{\tilde{\mathbf{k}}_0}$, can be defined by applying all symmetry operators $S \in G_{\tilde{\mathbf{k}}_0}$ to \mathbf{k}_0 and then collecting distinct momenta, namely

$$\tilde{A}_{\tilde{\mathbf{k}}_0} = \{\mathbf{k} | \exists S \in G_{\tilde{\mathbf{k}}_0}, \mathbf{k} = S\mathbf{k}_0\}. \quad (S2)$$

As $S \in O(3)$, all the momenta in one momentum shell $\tilde{A}_{\tilde{\mathbf{k}}_0}$ must have the same amplitude, and thus we can define the momentum shell amplitude as $|\tilde{A}_{\tilde{\mathbf{k}}_0}| = |\mathbf{k}_0|$. We arrange the momentum shells according to the ascending order of the momentum shell amplitude $|\tilde{A}_{\tilde{\mathbf{k}}_0}|$, and dub them as the 1st momentum shell, the 2nd momentum shell and so on. As an example, we consider the hexagonal MBZ in "Step 1" of Fig.S1, in which one can find only one momentum (green star) in \tilde{A}_Γ , six momenta (orange stars) in \tilde{A}_{Γ^1} , three momenta (green triangles) in \tilde{A}_K and three momenta (orange triangles) in \tilde{A}_{K^1} .

Step 2: the eigen-energy bands of $H_0(\mathbf{k}_0)$ at the momentum $\mathbf{k}_0 \in A_{\tilde{\mathbf{k}}_0}$ are folded into the momentum $\tilde{\mathbf{k}}_0$ in the 1st MBZ and the representation of the folded bands at $\tilde{\mathbf{k}}_0$ can be constructed under zero moiré potential $H_M = 0$. Here we consider a set of degenerate atomic energy bands, denoted as $|\Lambda_{\mathbf{k}_0}^0, n\rangle$, of H_0 at \mathbf{k}_0 in the ABZ with the eigen-energy $E_{\mathbf{k}_0}^\Lambda$. We further assume this set of basis wavefunctions belong to the irreducible representation (irrep) $\Lambda_{\mathbf{k}_0}^0$ of the group $G_{\tilde{\mathbf{k}}_0} \cap G_{\mathbf{k}_0}^0$, which is a subgroup of both $G_{\tilde{\mathbf{k}}_0}$ and $G_{\mathbf{k}_0}^0$. Here $n = 1, 2, \dots, N[\Lambda_{\mathbf{k}_0}^0]$ and $N[\Lambda_{\mathbf{k}_0}^0]$ labels the dimension of the irrep $\Lambda_{\mathbf{k}_0}^0$. For a symmetry operator $S_0 \in G_{\tilde{\mathbf{k}}_0} \cap G_{\mathbf{k}_0}^0$, its representation matrix $\mathcal{D}_{\mathbf{k}_0}^0(S_0)$ and the corresponding character $\chi_{\mathbf{k}_0}^0(S_0)$ are given by

$$S_0 |\Lambda_{\mathbf{k}_0}^0, n\rangle = \sum_{n'} |\Lambda_{\mathbf{k}_0}^0, n'\rangle \mathcal{D}_{\mathbf{k}_0, n'n}^0(S_0), \quad \chi_{\mathbf{k}_0}^0(S_0) = \text{Tr}[\mathcal{D}_{\mathbf{k}_0}^0(S_0)], \quad (S3)$$

as exemplified in Tab. S1(a). Next we consider the electronic bands at another different momentum $\mathbf{k}' = \mathcal{S}\mathbf{k}_0 \in \tilde{A}_{\mathbf{k}_0}$ with $\mathcal{S} \in G_{\tilde{\mathbf{k}}_0}$ and $\mathcal{S} \notin G_{\mathbf{k}_0}^0$ and construct the corresponding basis wavefunctions by $|\Lambda_{\mathbf{k}'}^0, n\rangle = \mathcal{S} |\Lambda_{\mathbf{k}_0}^0, n\rangle$, which are eigen-states of H_0 at \mathbf{k}' with the same eigen-energy,

$$H_0(\mathbf{k}') |\Lambda_{\mathbf{k}'}^0, n\rangle = \mathcal{S} H_0(\mathbf{k}_0) \mathcal{S}^{-1} \mathcal{S} |\Lambda_{\mathbf{k}_0}^0, n\rangle = E_{\mathbf{k}_0}^\Lambda |\Lambda_{\mathbf{k}'}^0, n\rangle. \quad (\text{S4})$$

As the basis wavefunctions at \mathbf{k}_0 and \mathbf{k}' are connected by symmetry operator, $|\Lambda_{\mathbf{k}'}^0, n\rangle$ must belong to the same irrep, denoted as $\Lambda_{\mathbf{k}'}^0$, as $|\Lambda_{\mathbf{k}_0}^0, n\rangle$. The characters of $\Lambda_{\mathbf{k}'}^0$ are summarized in Tab. S1(b). The wave vector group $G_{\mathbf{k}'}^0$ at \mathbf{k}' is isomorphic to $G_{\mathbf{k}_0}^0$ at \mathbf{k}_0 because for any $\mathcal{S}_0 \in G_{\mathbf{k}_0}^0$, the symmetry operator $\mathcal{S}'_0 = \mathcal{S} \mathcal{S}_0 \mathcal{S}^{-1}$ is an element in the wave vector group $G_{\mathbf{k}'}^0$ at \mathbf{k}' . The character of the symmetry operator \mathcal{S}'_0 in $\Lambda_{\mathbf{k}'}^0$, denoted as $\chi_{\mathbf{k}'}^0(\mathcal{S}'_0)$, should remain the same, namely $\chi_{\mathbf{k}'}^0(\mathcal{S}'_0) = \chi_{\mathbf{k}}^0(\mathcal{S}_0)$, because their representation matrices are the same,

$$\mathcal{D}_{\mathbf{k}', n_1 n_2}^0(\mathcal{S}'_0) = \langle \Lambda_{\mathbf{k}'}^0, n_1 | \mathcal{S}'_0 | \Lambda_{\mathbf{k}'}^0, n_2 \rangle = \langle \Lambda_{\mathbf{k}_0}^0, n_1 | \mathcal{S}^{-1} \mathcal{S}'_0 \mathcal{S} | \Lambda_{\mathbf{k}_0}^0, n_2 \rangle = \langle \Lambda_{\mathbf{k}_0}^0, n_1 | \mathcal{S}_0 | \Lambda_{\mathbf{k}_0}^0, n_2 \rangle = \mathcal{D}_{\mathbf{k}_0, n_1 n_2}^0(\mathcal{S}_0). \quad (\text{S5})$$

After the band folding, the atomic energy bands at all the momenta in one momentum shell will be folded into the same momentum in the MBZ, allowing us to construct the reducible representation of moiré minibands in the 1st MBZ based on atomic energy bands. More concretely, for a certain momentum $\mathbf{k}_0 \in A_{\tilde{\mathbf{k}}_0}$, we consider the band-folding for the atomic energy bands with the irrep $\Lambda_{\mathbf{k}_0}^0$. The bands with the irrep $\Lambda_{\mathbf{k}}^0$, which is isomorphic to the irrep $\Lambda_{\mathbf{k}_0}^0$, at all $\mathbf{k} \in \tilde{A}_{\mathbf{k}_0}$ are folded into the momentum $\tilde{\mathbf{k}}_0$ in the 1st MBZ to form an induced representation,

$$\tilde{\Lambda}_{\mathbf{k}_0} = \Lambda_{\mathbf{k}_0}^0 \uparrow G_{\tilde{\mathbf{k}}_0}, \quad (\text{S6})$$

where \uparrow is the induction of representation $\tilde{\Lambda}_{\mathbf{k}_0}$ in the group $G_{\tilde{\mathbf{k}}_0}$ from the representation $\Lambda_{\mathbf{k}_0}^0$ of the group $G_{\tilde{\mathbf{k}}_0} \cap G_{\mathbf{k}_0}^0 \subset G_{\tilde{\mathbf{k}}_0}$, as defined in TQC [39, 42, 61]. $\tilde{\Lambda}_{\mathbf{k}_0}$ is a reducible representation. The basis for the induced representation $\tilde{\Lambda}_{\mathbf{k}_0}$ are $|\Lambda_{\mathbf{k}}^0, n\rangle$ for all $\mathbf{k} \in \tilde{A}_{\mathbf{k}_0}$ and n , generated by acting all $\mathcal{S} \in G_{\tilde{\mathbf{k}}_0}$ on the $|\Lambda_{\mathbf{k}_0}^0, n\rangle$ in the irrep $\Lambda_{\mathbf{k}_0}^0$. As the irreps $\Lambda_{\mathbf{k}}^0$ for all $\mathbf{k} \in \tilde{A}_{\mathbf{k}_0}$ are transformed to each other by $\mathcal{S} \in G_{\tilde{\mathbf{k}}_0}$, $\tilde{\Lambda}_{\mathbf{k}_0}$ is just $N[\tilde{A}_{\mathbf{k}_0}]$ copies of $\Lambda_{\mathbf{k}_0}^0$, where $N[\tilde{A}_{\mathbf{k}_0}]$ is the number of different momenta in one momentum shell $\tilde{A}_{\mathbf{k}_0}$. The dimension of $\tilde{\Lambda}_{\mathbf{k}_0}$ is $N[\tilde{\Lambda}_{\mathbf{k}_0}] = N[\tilde{A}_{\mathbf{k}_0}] \times N[\Lambda_{\mathbf{k}_0}^0]$. The characters of symmetry operators of $G_{\tilde{\mathbf{k}}_0}$ in $\tilde{\Lambda}_{\mathbf{k}_0}$ are discussed in step 3 below.

Step 3: we decompose the reducible representation $\tilde{\Lambda}_{\mathbf{k}_0}$ into irreps of the wave vector group $G_{\tilde{\mathbf{k}}_0}$ of the moiré system using the character table. To decompose $\tilde{\Lambda}_{\mathbf{k}_0}$, we need to evaluate the character of $\tilde{\Lambda}_{\mathbf{k}_0}$, which can be directly connected to the characters of irreps $\Lambda_{\mathbf{k}}^0$ for all $\mathbf{k} \in \tilde{A}_{\mathbf{k}_0}$ via Eq. (S6). For a given $\mathcal{S} \in G_{\tilde{\mathbf{k}}_0}$ and a given $\tilde{\Lambda}_{\mathbf{k}_0}$ at the momentum $\mathbf{k}_0 \in A_{\tilde{\mathbf{k}}_0}$, we can classify all momenta $\mathbf{k} \in \tilde{A}_{\mathbf{k}_0}$ into two types: (1) $\mathcal{S} \in G_{\mathbf{k}}^0 \cap G_{\tilde{\mathbf{k}}_0}$ and (2) $\mathcal{S} \notin G_{\mathbf{k}}^0 \cap G_{\tilde{\mathbf{k}}_0}$. For type (1), the representation matrix $\mathcal{D}_{\mathbf{k}}^0(\mathcal{S})$ and the character $\chi_{\mathbf{k}}^0(\mathcal{S})$ are defined by Eq. (S3). For type (2), \mathbf{k} and $\mathbf{k}' = \mathcal{S}\mathbf{k}$ are two different momenta in $G_{\mathbf{k}}^0$, so all the diagonal components of the representation matrix for \mathcal{S} must be zero, leading to zero character. With the characters for both types of momenta, we have

$$\tilde{\chi}_{\mathbf{k}_0}(\mathcal{S}) = \sum_{\{\mathbf{k} | \mathbf{k} \in \tilde{A}_{\mathbf{k}_0}, \mathcal{S} \in G_{\mathbf{k}}^0 \cap G_{\tilde{\mathbf{k}}_0}\}} \chi_{\mathbf{k}}^0(\mathcal{S}). \quad (\text{S7})$$

Applying Eq.(S7) to all symmetry operators $\mathcal{S} \in G_{\tilde{\mathbf{k}}_0}$, we can construct the characters of all symmetry operators in $G_{\tilde{\mathbf{k}}_0}$ for the reducible representation $\tilde{\Lambda}_{\mathbf{k}_0}$, which allows us to decompose $\tilde{\Lambda}_{\mathbf{k}_0}$ through the character table according to the wonderful orthogonality theorem[74] into irreps $\Lambda_{\tilde{\mathbf{k}}_0, \alpha}$, where α labels different irreps, of $G_{\tilde{\mathbf{k}}_0}$,

$$\tilde{\Lambda}_{\mathbf{k}_0} = \oplus_{\alpha} c_{\alpha} \Lambda_{\tilde{\mathbf{k}}_0, \alpha} \quad (\text{S8})$$

with c_{α} as the multiple of irreps.

Step 4: we treat the weak moiré potential H_M as a perturbation and construct the effective Hamiltonian for the minibands with the irreps in $\tilde{\Lambda}_{\mathbf{k}_0}$. All the states in $\tilde{\Lambda}_{\mathbf{k}_0}$ are degenerate at zero moiré potential and the first-order perturbation of the moiré potential H_M in $\tilde{\Lambda}_{\mathbf{k}_0}$ is

$$(H_{M, \mathbf{k}_0}^{(1)})_{n_1 k_1, n_2 k_2} = \langle \Lambda_{\mathbf{k}_1}^0, n_1 | H_M | \Lambda_{\mathbf{k}_2}^0, n_2 \rangle \quad (\text{S9})$$

with $\mathbf{k}_1, \mathbf{k}_2 \in \tilde{A}_{\mathbf{k}_0}$. We can diagonalize the effective Hamiltonian $H_{M, \mathbf{k}_0}^{(1)}$ and the obtained eigen-states are characterized by the irreps $\Lambda_{\tilde{\mathbf{k}}_0, \alpha}$ of $G_{\tilde{\mathbf{k}}_0}$, which just corresponds to the representation decomposition in Eq.(S8). These eigen-states

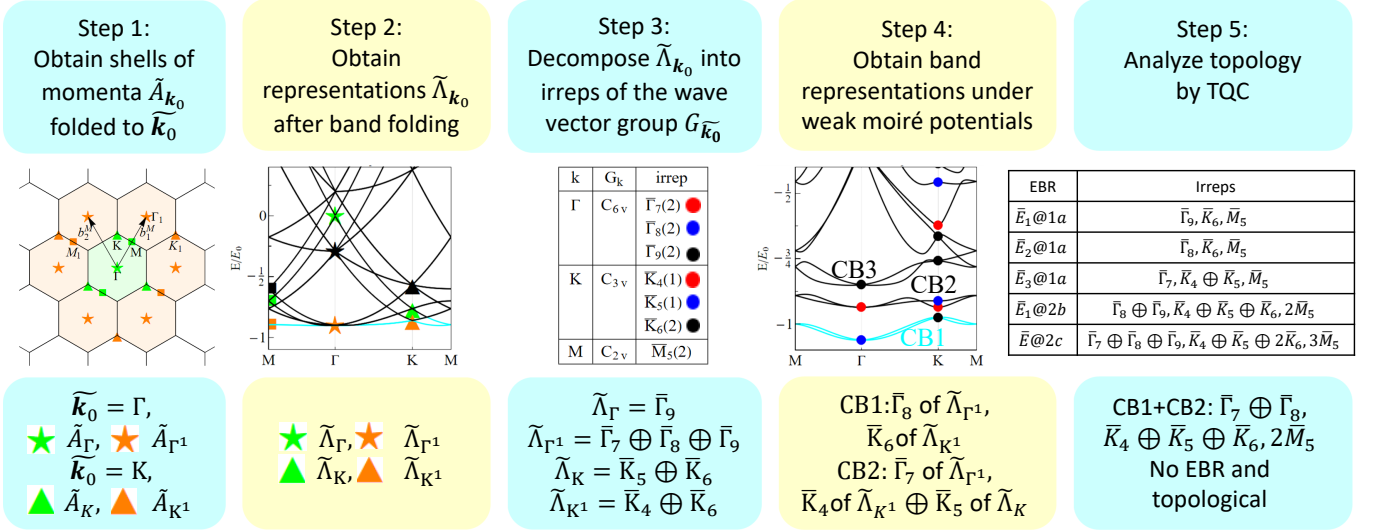


FIG. S1. The flow chart of moiré TQC with the moiré Rashba systems as an example. The first row are the goals for each step. The second row are figures for the moiré Rashba systems adapted from Fig. 1 and Fig. 2 in the main text. The table under the step 5 lists irreps at high symmetry points for all EBR in the space group $P6mm$. The third row is the results from each step.

(a)

$G_{\mathbf{k}_0}^0$	\mathcal{S}_0	\mathcal{S}_1	...
$\Lambda_{\mathbf{k}_0}^0$	$\chi_{\mathbf{k}_0}^0(\mathcal{S}_0)$	$\chi_{\mathbf{k}_0}^0(\mathcal{S}_1)$...

(b)

$G_{\mathbf{k}'}^0$	$\mathcal{S}'_0 = \mathcal{S}\mathcal{S}_0\mathcal{S}^{-1}$	$\mathcal{S}'_1 = \mathcal{S}\mathcal{S}_1\mathcal{S}^{-1}$...
$\Lambda_{\mathbf{k}'}^0$	$\chi_{\mathbf{k}'}^0(\mathcal{S}'_0) = \chi_{\mathbf{k}_0}^0(\mathcal{S}_0)$	$\chi_{\mathbf{k}'}^0(\mathcal{S}'_1) = \chi_{\mathbf{k}_0}^0(\mathcal{S}_1)$...

TABLE S1. (a) The characters of symmetry operators $\mathcal{S}_0, \mathcal{S}_1, \dots$ in the group $G_{\mathbf{k}_0}^0 \cap G_{\tilde{\mathbf{k}}_0}$ for the irrep $\Lambda_{\mathbf{k}_0}^0$. (b) The characters of symmetry operators in the group $G_{\mathbf{k}'}^0 \cap G_{\tilde{\mathbf{k}}_0}$ for the irrep $\Lambda_{\mathbf{k}'}^0$. $\mathbf{k}' = \mathcal{S}\mathbf{k}_0$ labels a momentum different from \mathbf{k}_0 , but is connected to \mathbf{k}_0 by a symmetry operator $\mathcal{S} \in G_{\tilde{\mathbf{k}}_0}$.

with different irreps at high symmetry momenta can be ordered in energy and connected along high symmetry lines to construct the band representations of moiré minibands by compatibility relations [39].

Step 5: we analyze the topology of the moiré minibands using the topological quantum chemistry method [39, 42, 61] by comparing the band representations of moiré minibands with the elementary band representation (EBR) from the Bilbao Crystallographic Server [39, 42, 61].

Although we discussed our formalism for the space groups only, time reversal symmetry can also be included in the context of magnetic space groups, and each step in our formalism is still applicable.

II. MOIRÉ RASHBA SYSTEMS

A. Moiré TQC analysis

In this section, we will apply our general formalism developed in Sec. I to the Rashba moiré system as an example to show that the band inversion between the states derived from the 1st and 2nd MBZ leads to the exchange of the states with different symmetry irreps at Γ and K , giving rise to nontrivial band topology. The results of each step in Sec. I is shown in Fig. S1, which will be described in details below.

Step 1: we first identify the momentum shells folded to Γ and K from the 1st and 2nd extended MBZ. The space group for the Rashba model is $G^0 = C_{\infty v} \otimes G^T$, where G^T is the continuous translation group and $C_{\infty v}$ is the full

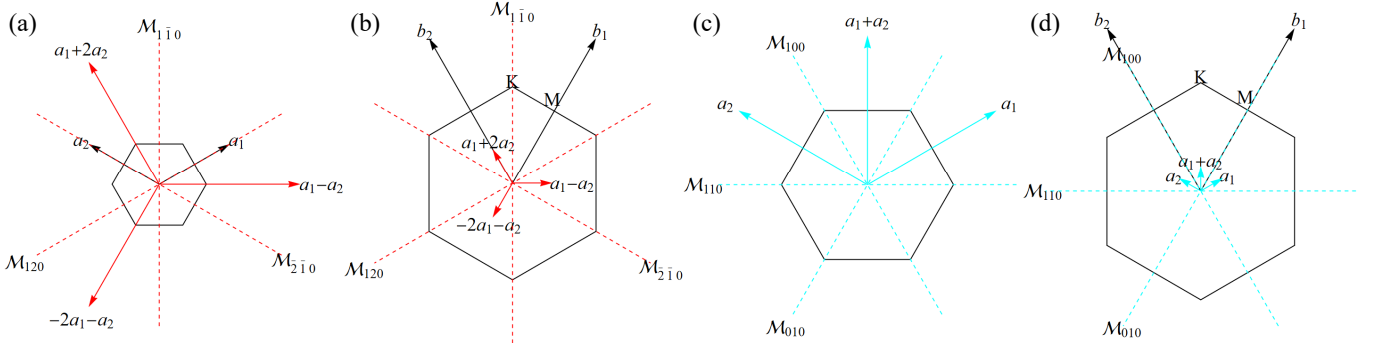


FIG. S2. (a) Mirror symmetries $\mathcal{M}_{120}, \mathcal{M}_{2\bar{1}0}, \mathcal{M}_{1\bar{1}0}$ in the real space. $\mathbf{a}_1, \mathbf{a}_2$ are the primitive lattice vectors. The red dashed lines are mirror planes of \mathcal{M}_{ij0} and the red arrows are normal vectors $i\mathbf{a}_1 + j\mathbf{a}_2$ perpendicular to the mirror plane. (b) Mirror symmetries $\mathcal{M}_{120}, \mathcal{M}_{2\bar{1}0}, \mathcal{M}_{1\bar{1}0}$ in the momentum space space. $\mathbf{b}_1, \mathbf{b}_2$ are the primitive reciprocal lattice vectors. $i\mathbf{a}_1 + j\mathbf{a}_2$ indicates the direction of the normal vector perpendicular to the mirror plane of \mathcal{M}_{ij0} . (c)(d) Mirror symmetries $\mathcal{M}_{110}, \mathcal{M}_{100}, \mathcal{M}_{010}$ in the real (momentum) space. The blue dashed lines are mirror planes of \mathcal{M}_{ij0} with the normal vector in the direction of blue arrows $i\mathbf{a}_1 + j\mathbf{a}_2$.

rotation group about z-axis together with in-plane mirrors. The space group G^M of the moiré potential H_M is chosen to be $P6/mmm$, corresponding to the point group D_{6h} [75]. The space group for the whole system is $P6mm$ from $G = G^M \cap G^0$ corresponding to the point group C_{6v} .

We first consider the momentum set A_Γ , namely the momenta \mathbf{k}_0 in ABZ that can be folded to $\tilde{\mathbf{k}}_0 = \Gamma$ in MBZ. The wave vector group at Γ for G is $G_\Gamma = C_{6v}$ with the symmetry operators, including the six-fold, three-fold, two-fold rotation symmetries about the z axis C_{6z}, C_{3z}, C_{2z} , respectively, and the mirror symmetries \mathcal{M}_{ij0} with the normal vector along the direction $i\mathbf{a}_1^M + j\mathbf{a}_2^M$ shown in the real space and momentum space in Fig. S2, where $\mathbf{a}_1^M = L_M(\sqrt{3}/2, 1/2)$, $\mathbf{a}_2^M = L_M(-\sqrt{3}/2, 1/2)$ are primitive vectors for the moiré unit cell. Here we follow the notation in the Bilbao Crystallographic Server [76, 77]. Tab. S2(a) gives the irreps only appearing in the double group of C_{6v} . In Tab. S2(a), symmetry operators belonging to one conjugacy class are put into the same column. From the definition of Eq. (S2), the first two momentum shells are given by

$$\begin{aligned} \tilde{A}_\Gamma &= \{\Gamma\} \\ \tilde{A}_{\Gamma^1} &= \{\pm\mathbf{b}_1^M, \pm\mathbf{b}_2^M, \pm(\mathbf{b}_1^M - \mathbf{b}_2^M)\}, \end{aligned} \quad (\text{S10})$$

where the primitive reciprocal lattice vectors are given by $\mathbf{b}_1^M = \frac{4\pi}{\sqrt{3}L_M}(\sqrt{3}/2, 1/2)$, $\mathbf{b}_2^M = \frac{4\pi}{\sqrt{3}L_M}(-\sqrt{3}/2, 1/2)$. The momenta in \tilde{A}_{Γ^1} are obtained from $\Gamma^1 = \mathbf{b}_1^M$ by

$$\mathbf{b}_2^M = C_{6z}\Gamma^1 \quad \mathbf{b}_2^M - \mathbf{b}_1^M = C_{3z}\Gamma^1 \quad -\mathbf{b}_1^M = C_{2z}\Gamma^1 \quad -\mathbf{b}_2^M = C_{3z}^{-1}\Gamma^1 \quad \mathbf{b}_1^M - \mathbf{b}_2^M = C_{6z}^{-1}\Gamma^1. \quad (\text{S11})$$

Next, we consider the momentum shells that are connected to K . The wave vector group at K is $G_K = C_{3v}$ with the symmetry operators and double group irreps listed in Tab. S3(a). Here we choose $K = \mathbf{b}_1^M/3 + \mathbf{b}_2^M/3$ in the 1st MBZ and $K^1 = 4\mathbf{b}_1^M/3 - 2\mathbf{b}_2^M/3$ in the 2nd MBZ to construct the first two momentum shells, following step 1 of Fig. S1. Similarly from Eq. (S2), the first two momentum shells are

$$\begin{aligned} \tilde{A}_K &= \{\mathbf{b}_1^M/3 + \mathbf{b}_2^M/3, -2\mathbf{b}_1^M/3 + \mathbf{b}_2^M/3, \mathbf{b}_1^M/3 - 2\mathbf{b}_2^M/3\} \\ \tilde{A}_{K^1} &= \{4\mathbf{b}_1^M/3 - \mathbf{b}_2^M/3, -2\mathbf{b}_1^M/3 + 4\mathbf{b}_2^M/3, -2\mathbf{b}_1^M/3 - 2\mathbf{b}_2^M/3\}. \end{aligned} \quad (\text{S12})$$

Step 2: we will derive the representations of states folded from $\tilde{A}_\Gamma, \tilde{A}_K$ in the 1st MBZ and $\tilde{A}_{\Gamma^1}, \tilde{A}_{K^1}$ in the 2nd MBZ. At Γ , the wave vector groups are $G_\Gamma^0 = C_{\infty v}$ of the unfolded Rashba model and $G_\Gamma = C_{6v}$ for the moiré systems. Thus, we choose the group $G_\Gamma^0 \cap G_\Gamma = C_{6v}$ to label atomic bands at Γ . The symmetry irrep of the unfolded Rashba model under $G_\Gamma^0 \cap G_\Gamma$ is $\Lambda_\Gamma^0 = \bar{\Gamma}_9^0$. Here we emphasize that we use the notation $\bar{\Gamma}$ (with a bar on top of the high symmetry momentum) to label the irreducible representation, which is different from Γ that labels the momentum, and we follow this convention below. The characters of symmetry operators in $\bar{\Gamma}_9^0$ are listed in Tab. S2(b). Since there is only Γ in \tilde{A}_Γ , the representations is $\tilde{A}_\Gamma = \bar{\Gamma}_9^0$ in MBZ. At Γ^1 , the unfolded Rashba model has the wave vector group $G_{\Gamma^1}^0 = C_m$ with only in-plane mirror symmetry \mathcal{M}_{010} . The irrep of the lower energy band of the unfolded Rashba model at Γ^1 is $\bar{\Gamma}_3^0$ with the characters $\chi_{\Gamma^1}^0(\mathcal{S}_0)$ for the symmetry operators \mathcal{S}_0 in the group $G_{\Gamma^1}^0 \cap G_\Gamma = C_m$ listed in

(a)	C_{6v}	ε	C_{6z}, C_{6z}^{-1}	C_{3z}, C_{3z}^{-1}	C_{2z}	$\mathcal{M}_{110}, \mathcal{M}_{100}, \mathcal{M}_{010}$	$\mathcal{M}_{1\bar{1}0}, \mathcal{M}_{120}, \mathcal{M}_{\bar{2}10}$
	$\bar{\Gamma}_7$	2	0	-2	0	0	0
	$\bar{\Gamma}_8$	2	$-\sqrt{3}$	1	0	0	0
	$\bar{\Gamma}_9$	2	$\sqrt{3}$	1	0	0	0
(b)	$G_\Gamma^0 \cap G_\Gamma$	ε	C_{6z}, C_{6z}^{-1}	C_{3z}, C_{3z}^{-1}	C_{2z}	$\mathcal{M}_{110}, \mathcal{M}_{100}, \mathcal{M}_{010}$	$\mathcal{M}_{1\bar{1}0}, \mathcal{M}_{120}, \mathcal{M}_{\bar{2}10}$
	$\bar{\Gamma}_9^0$	2	$\sqrt{3}$	1	0	0	0
(d)	G_Γ	ε	C_{6z}, C_{6z}^{-1}	C_{3z}, C_{3z}^{-1}	C_{2z}	$\mathcal{M}_{110}, \mathcal{M}_{100}, \mathcal{M}_{010}$	$\mathcal{M}_{1\bar{1}0}, \mathcal{M}_{120}, \mathcal{M}_{\bar{2}10}$
	$\tilde{\Lambda}_\Gamma$	2	$\sqrt{3}$	1	0	0	0
(e)	G_Γ	ε	C_{6z}, C_{6z}^{-1}	C_{3z}, C_{3z}^{-1}	C_{2z}	$\mathcal{M}_{110}, \mathcal{M}_{100}, \mathcal{M}_{010}$	$\mathcal{M}_{1\bar{1}0}, \mathcal{M}_{120}, \mathcal{M}_{\bar{2}10}$
	$\tilde{\Lambda}_{\Gamma^1}$	6	0	0	0	0	0
(c)	$G_{\Gamma^1}^0 \cap G_\Gamma$	ε	\mathcal{M}_{010}				
	$\bar{\Gamma}_3^0$	1	$-i$				
	$G_{-b_1^M}^0$	$\varepsilon = C_{2z} \varepsilon C_{2z}^{-1}$		$\mathcal{M}_{010} = C_{2z} \mathcal{M}_{010}^{-1} C_{2z}^{-1}$			
	$-\bar{b}_1^M$	1	$+i$				
(f)	$G_{\Gamma^1}^0 \cap G_\Gamma$	ε	\mathcal{M}_{010}				
	$\bar{\Gamma}_4^0$	1	$+i$				

TABLE S2. (a) The character table for the wave vector group $G_\Gamma = C_{6v}$. (b) The characters of symmetry operators in the group $G_\Gamma^0 \cap G_\Gamma = C_{6v}$ for the irrep Λ_Γ^0 of the unfolded Rashba model at Γ . (c) The characters of the symmetry operators in the group $G_{\Gamma^1}^0 \cap G_\Gamma = C_m (G_{-b_1^M}^0 \cap G_\Gamma = C_m)$ for the irrep $\Lambda_{\Gamma^1}^0 (\Lambda_{-b_1^M}^0)$ of the unfolded Rashba model at $\Gamma^1 (-b_1^M)$. $\Gamma^1 = b_1^M, -b_1^M$ are two momenta invariant under \mathcal{M}_{010} . (d)(e) The characters of the symmetry operators in the group G_Γ for the folded representations $\tilde{\Lambda}_\Gamma, \tilde{\Lambda}_{\Gamma^1}$. (f) The characters of the symmetry operators in the group $G_{\Gamma^1}^0 \cap G_\Gamma$ for the irrep $\bar{\Gamma}_4^0$ of the unfolded Rashba model at Γ^1 .

(a)	C_{3v}	ε	C_{3z}, C_{3z}^{-1}	$\mathcal{M}_{1\bar{1}0}, \mathcal{M}_{120}, \mathcal{M}_{\bar{2}10}$
	\bar{K}_4	1	-1	$-i$
	\bar{K}_5	1	-1	$+i$
	\bar{K}_6	2	1	0
(b)	$G_K^0 \cap G_K$	ε	$\mathcal{M}_{1\bar{1}0} = \mathcal{M}_{\bar{1}10}^{-1}$	
	\bar{K}_4^0	1	$+i$	
(c)	$G_{K^1}^0 \cap G_K$	ε	\mathcal{M}_{120}	
	\bar{K}_3^0	1	$-i$	
(d)	G_K	ε	C_{3z}, C_{3z}^{-1}	$\mathcal{M}_{1\bar{1}0}, \mathcal{M}_{120}, \mathcal{M}_{\bar{2}10}$
	$\tilde{\Lambda}_K$	3	0	$+i$
(e)	G_K	ε	C_{3z}, C_{3z}^{-1}	$\mathcal{M}_{1\bar{1}0}, \mathcal{M}_{120}, \mathcal{M}_{\bar{2}10}$
	$\tilde{\Lambda}_{K^1}$	3	0	$-i$

TABLE S3. (a) The character table for the wave vector group $G_K = C_{3v}$. (b)(c) The characters of symmetry operators in the group $G_K^0 \cap G_K = C_m (G_{K^1}^0 \cap G_K = C_m)$ for the irrep $\Lambda_K^0 = \bar{K}_4^0 (\Lambda_{K^1}^0 = \bar{K}_3^0)$ of the unfolded Rashba model at K . (d)(e) The characters of symmetry operators in the group G_K for folded representations $\tilde{\Lambda}_K (\tilde{\Lambda}_{K^1})$.

Tab. S2(c). Along the line $\Gamma - \Gamma^1$, $\bar{\Gamma}_9^0$ splits by $\bar{\Gamma}_9^0 = \bar{\Gamma}_3^0 \oplus \bar{\Gamma}_4^0$, where $\bar{\Gamma}_3^0$ and $\bar{\Gamma}_4^0$ are two double group irreps at Γ^1 with opposite mirror eigenvalues $-i$ and $+i$, respectively, under the mirror operator \mathcal{M}_{010} with the characters listed in Tab. S2(c)(f). The Rashba Hamiltonian is $H_R(\mathbf{k}) = ak^2 \sigma_0 - \lambda(\mathbf{k} \times \boldsymbol{\sigma}) \cdot \hat{z}$ as Eq. (1) in the main text and the mirror symmetry operator with the mirror plane normal vector $\hat{z} \times \hat{k}$ is $\mathcal{M}_{\hat{z} \times \hat{k}} = -i(\hat{z} \times \hat{k}) \cdot \boldsymbol{\sigma}$, where \hat{z}, \hat{k} are unit vectors along the z, \mathbf{k} direction, respectively. For the Rashba strength $\lambda > 0$, we find $\bar{\Gamma}_3^0$ with the mirror eigenvalue $-i$ has the lower energy $a|\mathbf{b}_1^M|^2 - \lambda|\mathbf{b}_1^M|$. Next, the characters at $\mathbf{k}' \in \tilde{\Lambda}_{\Gamma^1}$ of $\Lambda_{\mathbf{k}'}^0$ are derived in the Tab. S2(c) following Tab. S1. From Eq. (S6), we obtain $\tilde{\Lambda}_{\Gamma^1} = \Lambda_{\Gamma^1}^0 \uparrow G_\Gamma$.

Similarly, at K, K^1 , the unfolded Rashba model has the wave vector group $G_K \cap G_K^0 = G_K \cap G_{K^1}^0 = C_m$ and the corresponding representations $\tilde{\Lambda}_K, \tilde{\Lambda}_{K^1}$ can be constructed from the irreps \bar{K}_4^0, \bar{K}_3^0 at $\tilde{A}_K, \tilde{A}_{K^1}$ with their characters given in Tab. S3.

Step 3: we decompose the representation $\tilde{\Lambda}_\Gamma, \tilde{\Lambda}_{\Gamma^1}$ into irreps of the wave vector group G_Γ at Γ and $\tilde{\Lambda}_K, \tilde{\Lambda}_{K^1}$ into irreps of the wave vector group G_K at K using the character table. We evaluate the characters for the representations

$\tilde{\Lambda}_\Gamma$ and $\tilde{\Lambda}_{\Gamma^1}$ in Tab. S2(d) and (e), and then decompose them into irreps according to the character table of $G_\Gamma = C_{6v}$ in Tab. S2(a). For $\tilde{\Lambda}_\Gamma$, $\tilde{\chi}_\Gamma(\mathcal{S}) = \chi_\Gamma^0(\mathcal{S})$ for $\mathcal{S} \in G_\Gamma = C_{6v}$ using Eq. (S7), as shown in Tab. S2(d). By comparing Tab. S2(d) with the character table in Tab. S2(a), the wonderful orthogonality theorem gives

$$\tilde{\Lambda}_\Gamma = \bar{\Gamma}_9. \quad (\text{S13})$$

For $\tilde{\Lambda}_{\Gamma^1}$, the characters of all symmetry operators in the wave vector group G_Γ are summarized in Tab. S2(e). Below we take the characters $\tilde{\chi}_{\Gamma^1}(\mathcal{E})$ and $\tilde{\chi}_{\Gamma^1}(\mathcal{M}_{010})$ as examples. The identity operator \mathcal{E} appears in $G_\Gamma^0 \cap G_\Gamma$ for any $\mathbf{k} \in \tilde{A}_{\Gamma^1}$, and thus $\tilde{\chi}_{\Gamma^1}(\mathcal{E}) = 6$ from Eq. (S7), as there are six momenta in \tilde{A}_{Γ^1} . For the symmetry operator \mathcal{M}_{010} , only the momenta $\Gamma^1 = \mathbf{b}_1^M$ and $-\mathbf{b}_1^M$ are invariant, while the other momenta in \tilde{A}_{Γ^1} (Eq. S46) are not invariant. The mirror eigen-values for the irrep $\bar{\Gamma}_3^0$ and $-\bar{\mathbf{b}}_1^M$ are $-i$ and $+i$, respectively. Thus, we conclude $\tilde{\chi}_{\Gamma^1}(\mathcal{M}_{010}) = 0$ from Eq. (S7). $\mathcal{M}_{100}, \mathcal{M}_{110}, \mathcal{M}_{100}^{-1}, \mathcal{M}_{110}^{-1}$ belong to the same conjugacy class in G_Γ and appear in the same column in Tab. S2(c). The characters for other symmetry operators in G_Γ can be constructed in a similar manner. By comparing Tab. S2(e) and Tab. S2(a), the wonderful orthogonality theorem gives

$$\tilde{\Lambda}_{\Gamma^1} = \bar{\Gamma}_7 \oplus \bar{\Gamma}_8 \oplus \bar{\Gamma}_9. \quad (\text{S14})$$

Next, $\tilde{\Lambda}_K, \tilde{\Lambda}_{K^1}$ is decomposed with the character table in Tab. S3(d)(e) derived from Tab. S3(b)(c) following Eq. (S7). By comparing Tab. S3(d)(e) and Tab. S3(a), we obtain

$$\tilde{\Lambda}_K = \bar{K}_5 \oplus \bar{K}_6, \quad \tilde{\Lambda}_{K^1} = \bar{K}_4 \oplus \bar{K}_6. \quad (\text{S15})$$

Step 4: we write down effective Hamiltonian for the mini-bands of each irrep obtained from Step 3 at high symmetry momenta by treating the moiré potential with the perturbation theory, solve the eigen-energy problem for the effective Hamiltonian of each irrep, arrange them in energy and then connect them into energy bands. Starting from the unperturbed Rashba model in Eq. (1) of the main text, the energies and eigenstates are

$$|\mathbf{k}, \pm\rangle = \frac{1}{\sqrt{2}} \begin{pmatrix} 1 \\ \mp \frac{ik_x - k_y}{k} \end{pmatrix}, \quad E_R(\mathbf{k}, \pm) = ak^2 \pm \lambda k. \quad (\text{S16})$$

As the first momentum shell \tilde{A}_Γ only has one momentum, H_M does not split the degeneracy of $\tilde{\Lambda}_\Gamma$ protected by the time reversal \mathcal{T} . Thus, the irrep $\tilde{\Lambda}_\Gamma$ has the energy

$$E_\Gamma(\bar{\Gamma}_9) = 0 \quad (\text{S17})$$

for both spin states.

In contrast, H_M can split the degenerate states folded from the 2nd momentum shell \tilde{A}_{Γ^1} . We consider the lower eigen-energy state $|\mathbf{k}, -\rangle$ of H_R in Eq. (S16), and on the basis $|\mathbf{b}_1^M, -\rangle, |\mathbf{b}_2^M, -\rangle, |\mathbf{b}_2^M - \mathbf{b}_1^M, -\rangle, |-\mathbf{b}_1^M, -\rangle, |-\mathbf{b}_2^M, -\rangle, |\mathbf{b}_1^M - \mathbf{b}_2^M, -\rangle$, we can evaluate the matrix element $\langle \mathbf{k}_1, - | H_R + H_M | \mathbf{k}_2, - \rangle$ and construct effective Hamiltonian for the irrep $\tilde{\Lambda}_{\Gamma^1}$ as

$$H_{\Gamma^1} = \begin{pmatrix} E_R(\mathbf{b}_1^M, -) & \Delta_1 e^{i\pi/6} \sqrt{3}/2 & 0 & 0 & 0 & \Delta_1 e^{-i\pi/6} \sqrt{3}/2 \\ \Delta_1 e^{-i\pi/6} \sqrt{3}/2 & E_R(\mathbf{b}_2^M, -) & \Delta_1 e^{i\pi/6} \sqrt{3}/2 & 0 & 0 & 0 \\ 0 & \Delta_1 e^{-i\pi/6} \sqrt{3}/2 & E_R(\mathbf{b}_2^M - \mathbf{b}_1^M, -) & \Delta_1 e^{i\pi/6} \sqrt{3}/2 & 0 & 0 \\ 0 & 0 & \Delta_1 e^{-i\pi/6} \sqrt{3}/2 & E_R(-\mathbf{b}_1^M, -) & \Delta_1 e^{i\pi/6} \sqrt{3}/2 & 0 \\ 0 & 0 & 0 & \Delta_1 e^{-i\pi/6} \sqrt{3}/2 & E_R(-\mathbf{b}_2^M, -) & \Delta_1 e^{i\pi/6} \sqrt{3}/2 \\ \Delta_1 e^{i\pi/6} \sqrt{3}/2 & 0 & 0 & 0 & \Delta_1 e^{-i\pi/6} \sqrt{3}/2 & E_R(\mathbf{b}_1^M - \mathbf{b}_2^M, -) \end{pmatrix}, \quad (\text{S18})$$

where $\mathbf{k}_1, \mathbf{k}_2 \in \tilde{A}_{\Gamma^1}$ and $E_R(\Gamma^1, -) = a|\mathbf{b}_1^M|^2 - \lambda|\mathbf{b}_1^M|$. The eigen-energies of H_{Γ^1} are

$$E_{\Gamma^1}(\bar{\Gamma}_8) = E_R(\Gamma^1, -) - 3\Delta_1/2 \quad E_{\Gamma^1}(\bar{\Gamma}_7) = E_R(\Gamma^1, -) \quad E_{\Gamma^1}(\bar{\Gamma}_9) = E_R(\Gamma^1, -) + 3\Delta_1/2 \quad (\text{S19})$$

with double degeneracy as required by time reversal. Here $\bar{\Gamma}_{7,8,9}$ in the bracket after E_{Γ^1} gives the irrep for each eigen-state, which can be determined from the eigen-values of C_{6z} with the transformation matrix

$$C_{6z}(\tilde{\Lambda}_{\Gamma^1}) = \begin{pmatrix} 0 & 0 & 0 & 0 & 0 & e^{-i\pi/6} \\ e^{-i\pi/6} & 0 & 0 & 0 & 0 & 0 \\ 0 & e^{-i\pi/6} & 0 & 0 & 0 & 0 \\ 0 & 0 & e^{-i\pi/6} & 0 & 0 & 0 \\ 0 & 0 & 0 & e^{-i\pi/6} & 0 & 0 \\ 0 & 0 & 0 & 0 & e^{-i\pi/6} & 0 \end{pmatrix}. \quad (\text{S20})$$

$G_{\Gamma K} = C_m$	\mathcal{E}	$\mathcal{M}_{1\bar{1}0}$
$\bar{\Gamma}\bar{K}_3$	1	$-i$
$\bar{\Gamma}\bar{K}_4$	1	$+i$

TABLE S4. The character table for the wave vector group $G_{\Gamma K} = C_m$.

The eigen-energy splittings of the $\tilde{\Lambda}_{\Gamma^1}$ states from the above Hamiltonian H_{Γ^1} are consistent with the representation decomposition in Eq.(S14). For $\Delta_1 > 0$, the minibands with the irrep $\bar{\Gamma}_8$ have the lowest energy for $\tilde{\Lambda}_{\Gamma^1}$, which is consistent with the Fig. 2f in the main text.

Next, we determine the energy order of minibands with different irreps in $\tilde{\Lambda}_K, \tilde{\Lambda}_{K^1}$. At K , the first order perturbation Hamiltonian of H_M in the basis of states at \tilde{A}_K is

$$H_K = \begin{pmatrix} E_R(K, -) & \Delta_1 e^{i\pi/3}/2 & \Delta_1 e^{-i\pi/3}/2 \\ \Delta_1 e^{-i\pi/3}/2 & E_R(-\mathbf{b}_1^M/2/3 + \mathbf{b}_1^M/3, -) & \Delta_1 e^{i\pi/3}/2 \\ \Delta_1 e^{i\pi/3}/2 & \Delta_1 e^{-i\pi/3}/2 & E_R(\mathbf{b}_1^M/3 - \mathbf{b}_1^M/2/3, -) \end{pmatrix}, \quad (\text{S21})$$

where $E_R(K, -) = a|\mathbf{b}_1^M/3 + \mathbf{b}_2^M/3|^2 - \lambda|\mathbf{b}_1^M/3 + \mathbf{b}_2^M/3|$. The energies of H_K are

$$E_K(\bar{K}_5) = E_R(K, -) - \Delta_1 \quad E_K(\bar{K}_6) = E_R(K, -) + \Delta_1. \quad (\text{S22})$$

Here the $E_K(\bar{K}_5)$ state has no degeneracy while the $E_K(\bar{K}_6)$ states are doubly degenerate. For $\Delta_1 > 0$, $E_K(\bar{K}_5) < E_K(\bar{K}_6)$.

At K^1 , the first order perturbation Hamiltonian of H_M in the basis of states at \tilde{A}_{K^1} is zero because we made the first momentum shell approximation for H_M , so that $\mathbf{k}_2 - \mathbf{k}_1$ is not within the \mathbf{g} summation in H_M (Eq.2) of the main text for any $\mathbf{k}_1, \mathbf{k}_2 \in \tilde{A}_{K^1}$. Thus, we need to consider the second order perturbation to get the effective Hamiltonian,

$$(H_{K^1})_{\mathbf{k}_1, \mathbf{k}_2} = \langle \mathbf{k}_1, - | H_R | \mathbf{k}_2, - \rangle + \sum_{\mathbf{g} \in \{\pm \mathbf{b}_1^M, \pm \mathbf{b}_2^M, \pm(\mathbf{b}_1^M - \mathbf{b}_2^M)\}, n=\pm} \frac{\langle \mathbf{k}_1, - | H_M | \mathbf{k}_1 + \mathbf{g}, n \rangle \langle \mathbf{k}_1 + \mathbf{g}, n | H_M | \mathbf{k}_2, - \rangle}{E_R(K^1, -) - E_R(\mathbf{k}_1 + \mathbf{g}, n)},$$

$$H_{K^1} = \begin{pmatrix} E_R(K^1, -) + \Delta_1^2 f_d^{(2)}(K^1) & \Delta_1^2 e^{i\pi/3} f_{od}^{(2)}(K^1) & \Delta_1^2 e^{-i\pi/3} f_{od}^{(2)}(K^1) \\ \Delta_1^2 e^{-i\pi/3} f_{od}^{(2)}(K^1) & E_R(-\mathbf{b}_1^M/2/3 - \mathbf{b}_2^M/4/3, -) + \Delta_1^2 f_d^{(2)}(K^1) & \Delta_1^2 e^{i\pi/3} f_{od}^{(2)}(K^1) \\ \Delta_1^2 e^{i\pi/3} f_{od}^{(2)}(K^1) & \Delta_1^2 e^{-i\pi/3} f_{od}^{(2)}(K^1) & E_R(-\mathbf{b}_1^M/2/3 - \mathbf{b}_2^M/2/3, -) + \Delta_1^2 f_d^{(2)}(K^1) \end{pmatrix}, \quad (\text{S23})$$

where $\mathbf{k}_1, \mathbf{k}_2 \in \tilde{A}_{K^1}$, $E_R(K^1, -) = a|4\mathbf{b}_1^M/3 - \mathbf{b}_2^M/3|^2 - \lambda|4\mathbf{b}_1^M/3 - \mathbf{b}_2^M/3|$, and

$$f_{od}^{(2)}(K^1) = \frac{3}{4} \frac{1}{E_R(K^1, -) - E_R(K, -)} - \frac{1}{4} \frac{1}{E_R(K^1, -) - E_R(K, +)}$$

$$f_d^{(2)}(K^1) = \sum_{\mathbf{g} \in \{\pm \mathbf{b}_1^M, \pm \mathbf{b}_2^M, \pm(\mathbf{b}_1^M - \mathbf{b}_2^M)\}, n=\pm} \frac{\langle K^1, - | K^1 + \mathbf{g}, n \rangle \langle K^1 + \mathbf{g}, n | K^1, - \rangle}{E_R(K^1, -) - E_R(K^1 + \mathbf{g}, n)}. \quad (\text{S24})$$

The energies of H_{K^1} are

$$E_{K^1}(\bar{K}_4) = E_R(K^1, -) + \Delta_1^2 f_d^{(2)}(K^1) - 2\Delta_1^2 f_{od}^{(2)}(K^1) \quad E_K(\bar{K}_6) = E_R(K^1, -) + \Delta_1^2 f_d^{(2)}(K^1) + \Delta_1^2 f_{od}^{(2)}(K^1). \quad (\text{S25})$$

In the weak moiré potential limit $\Delta_1 \rightarrow 0$, when the $\tilde{\Lambda}_{K^1}$ states from the 2nd momentum shell with the dominant energy $E_R(K^1, -)$ and the $\tilde{\Lambda}_K$ states from the 1st momentum shell with $E_R(K, -)$ exchange in energy, $f_{od}^{(2)}(K^1)$ has a sign change as the energy difference $E_R(K^1, -) - E_R(K, -)$ appears in the denominator of Eq.(S24), so that $E_{K^1}(\bar{K}_4)$ and $E_{K^1}(\bar{K}_6)$ in $\tilde{\Lambda}_{K^1}$ also exchange their energy orders. For $E_R(K^1, -) < E_R(K, -) < E_R(K, +)$, $f_{od}^{(2)}(K^1) < 0$ and $E_{K^1}(\bar{K}_4) > E_{K^1}(\bar{K}_6)$. This corresponds to the blue region after the phase transition depicted by the black line at $L_M = 4L_R$ in Fig. 2a of main text.

Next, different irrep states at high symmetry momenta are connected into bands by the compatibility relation. According to the compatibility relation along the $\Gamma - K$ line, all double group irreps $\bar{\Gamma}_7, \bar{\Gamma}_8, \bar{\Gamma}_9$ at Γ are split into

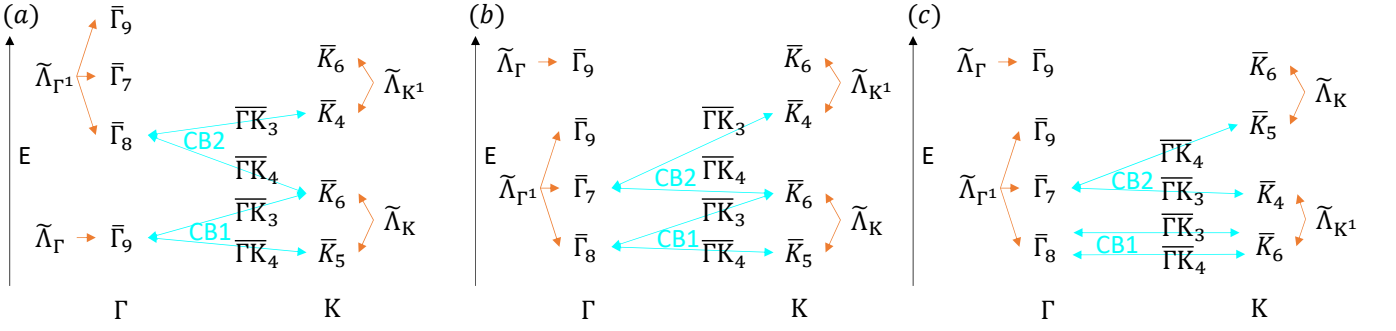


FIG. S3. (a)(b)(c) The irreps at Γ, K for the lowest two conduction minibands CB1 and CB2 determined by the compatibility relation for the parameter $1/\sqrt{3} < \sqrt{3}L_M/4L_R < 1, 1 < \sqrt{3}L_M/4L_R < \sqrt{3}, \sqrt{3} < \sqrt{3}L_M/4L_R$, respectively. The orange lines are the split of the folded representations by a weak moiré potential. The blue lines connect the irreps at Γ, K through the same irrep at the $\Gamma - K$ line, namely the compatibility relation.

$\overline{\Gamma K}_3 \oplus \overline{\Gamma K}_4$ and $\overline{K}_4, \overline{K}_5, \overline{K}_6$ becomes $\overline{\Gamma K}_3, \overline{\Gamma K}_4, \overline{\Gamma K}_3 \oplus \overline{\Gamma K}_4$, respectively. Here we use the notation $\overline{\Gamma K}$ to label the irreps along the $\Gamma - K$ lines. The character table for the wave vector group of momenta at $\Gamma - K$ is listed in Tab. S4. The irreps at Γ, K for different Rashba SOC strength are connected as shown in Fig. S3. Here we focus on the band connection of the lowest conduction bands, denoted as CB1, and the second lowest conduction bands, denoted as CB2, based on the above discussion on compatibility relation. For a small Rashba SOC parameter $\lambda \ll 1$ (or equivalently $L_M/L_R \ll 1$), the irrep at Γ for the lowest energy miniband CB1 comes from $\tilde{\Lambda}_\Gamma$ that belong to the $\tilde{\Gamma}_9$ irrep and the irrep at K comes from $\tilde{\Lambda}_K$ with two irreps \overline{K}_5 and \overline{K}_6 . For $\Delta_1 > 0$, $E_K(\overline{K}_5) < E_K(\overline{K}_6)$ so that the lowest energy bands at K belong to the 1D \overline{K}_5 irrep. The 2D irrep $\tilde{\Gamma}_9$ from $\tilde{\Lambda}_\Gamma$ is connected to 1D \overline{K}_5 for one state while the other state in $\tilde{\Gamma}_9$ is connected to one state in 2D \overline{K}_6 in $\tilde{\Lambda}_K$, forming the band representations of CB1. Thus, CB1 must have band touching with higher energy minibands, which is shown as the semimetal phase in the phase diagram for Fig.2a of the main text. When the Rashba parameter λ is increased so that $1/\sqrt{3} < \sqrt{3}L_M/4L_R < 1$, $E_R(K, +) > E_R(K^1, -)$, and the irreps $\tilde{\Gamma}_9$ from $\tilde{\Lambda}_\Gamma$ and $\tilde{\Gamma}_8$ from $\tilde{\Lambda}_{\Gamma^1}$ are connected to \overline{K}_5 and \overline{K}_6 from $\tilde{\Lambda}_K$ and \overline{K}_4 from $\tilde{\Lambda}_{K^1}$ as shown in Fig. S3(a), so that the CB1 still have band touching with CB2 and thus remains in the semi-metal phase. However, the band character of CB2 is changed due to the band inversion between the $E_R(K, +)$ bands and $E_R(K^1, -)$ bands, as compared to the case of $L_M/L_R \ll 1$. The miniband inversion from different momentum shells first occurs at Γ between the $\tilde{\Lambda}_\Gamma$ state from the 1st MBZ and the $\tilde{\Lambda}_{\Gamma^1}$ states from the 2nd MBZ for $\sqrt{3}L_M/4L_R = 1$. As shown in Fig. S3(b), when $1 < \sqrt{3}L_M/4L_R < \sqrt{3}$, the $\tilde{\Gamma}_8$ and $\tilde{\Gamma}_7$ states from $\tilde{\Lambda}_{\Gamma^1}$ have lower energy than the $\tilde{\Lambda}_\Gamma$ states, so they are connected to $\overline{K}_5, \overline{K}_6$ from $\tilde{\Lambda}_K$ and \overline{K}_4 from $\tilde{\Lambda}_{K^1}$, forming the band representations of CB1 and CB2, which are still connected via band touching. With further increasing the Rashba SOC λ , the miniband inversion from different momentum shells occurs at K , between the $\tilde{\Lambda}_K$ states from the 1st momentum shell and the $\tilde{\Lambda}_{K^1}$ states from the 2nd momentum shell for $\sqrt{3}L_M/4L_R = \sqrt{3}$. As shown in Fig. S3(c), when $\sqrt{3}L_M/4L_R > \sqrt{3}$, the $\tilde{\Lambda}_{K^1}$ states have the lower energy than the $\tilde{\Lambda}_K$ states and the 2D irrep \overline{K}_6 states have the lowest energy. The 2D irrep $\tilde{\Gamma}_8$ from $\tilde{\Lambda}_{\Gamma^1}$ is connected to the 2D \overline{K}_6 from $\tilde{\Lambda}_{K^1}$, forming the band representations of CB1, which are isolated from other minibands, as shown in Fig. S3(c). The band representation of CB1 corresponds to the blue region of Fig. 2(a) of the main text, in which the irrep at Γ for the lowest energy miniband CB1 comes from $\tilde{\Lambda}_{\Gamma^1}$ and the irrep at K comes from $\tilde{\Lambda}_{K^1}$.

Step 5: we compare the band representations at high symmetry points shown in Fig. S3 with EBR to determine its topology. For Fig. S3(a), as the $\tilde{\Gamma}_9$ irrep for the lowest energy states at Γ is 2D while the \overline{K}_5 irrep at K is 1D, CB1 has to be connected to CB2 (the second lowest energy band) at K , thus forming a semi-metal phase. CB1 and CB2 together form a band representation that is the same as the EBR $\tilde{E}_1@2b$ listed in the table of the step 5 in Fig. S1. Therefore, we expect the CB1 and CB2 together to be topologically trivial. In Fig. S3(b) after the band inversion between $\tilde{\Lambda}_\Gamma$ and $\tilde{\Lambda}_{\Gamma^1}$ at Γ , CB1 is still in the semi-metal phase. CB1 and CB2 together do not correspond to any EBR and thus become topological after band inversion. In this sense, it is a topological phase transition due to the irrep exchange between the 1st MBZ and 2nd MBZ at Γ . For Fig. S3(c) after the band inversion between $\tilde{\Lambda}_K$ and $\tilde{\Lambda}_{K^1}$ at K , CB1 becomes isolated and has the same irreps as EBR $\tilde{E}_2@1a$. However, in this case CB1 is still topologically nontrivial, which can be characterized by nontrivial \mathbb{Z}_2 number, as shown by the Wannier center flow in 2(f) of the main text. The irreps of CB1 and CB2 together do not change and are still \mathbb{Z}_2 non-trivial.

material	$\lambda(\text{eV}\text{\AA})$	$\mu(\text{cm}^2/\text{Vs})$	m	$L_R(\text{nm})$	$E_0(\text{meV})$	$E_\tau(\text{meV})$
GaAs/AlGaAs (111)	0.0055	1.455×10^6	$0.067m_0$	3750	0.0004	0.012
InAs quantum well	0.4	2.15×10^5	$0.036m_0$	96	1.13	0.15
InAs/GaSb	0.09	1.00×10^5	$0.055m_0$	279	0.088	0.21
InGaAs/InAlAs	0.04	1.34×10^5	$0.04m_0$	864	0.013	0.22
InAs/AlSb	0.06	1.22×10^5	$0.023m_0$	1001	0.016	0.41

TABLE S5. Promising Rashba semiconductor heterostructures for the moiré Rashba model. λ , μ , m , L_R , E_0 , and E_τ are the Rashba SOC, mobility, effective mass, spin precession length, miniband energy scale, and disorder broadening energy scale, respectively. $a = \hbar^2/2m$ in Eq. (1) of the main text. $E_0 = a(\pi/L_R)^2$ is the energy scale for the minibands when the band inversion between spectra folded from 1st and 2nd MBZ happens. $E_\tau = e\hbar/\mu m$ is the disorder broadening.

B. Material realization

Finally, we discuss the possible material realization of the moiré Rashba system. The Rashba materials are very common in 2D semiconductor heterostructures with electron gases. In certain types of systems, the Rashba strength can be large and easily tuned by the displacement field of external gate voltages. Meanwhile, high mobility in 2D semiconductor heterostructures can potentially support large moiré unit cell length L_M to be comparable to L_R for the band-folding mechanism to work. In Tab. S5 we summarized the promising semiconductor heterostructures with Rashba SOC [78–86]. Taking the InAs quantum well [81] as an example, it has $L_R \sim 96\text{nm}$ and the corresponding energy scale $E_0 \sim a/L_R^2 \sim 1.1\text{meV}$. Patterning hole arrays in substrates allow for a superlattice potential with the unit cell length $L_M \gtrsim 40\text{nm}$ and tunable superlattice potential strength up to $\Delta_1 \sim 10\text{meV}$ [71, 72]. Thus, the moiré length scale L_M and the Rashba length L_R can be comparable. Furthermore, the high mobility in InAs quantum wells guarantees a small disorder broadening $E_\tau \sim 0.15\text{meV}$, which is much smaller than E_0 and Δ_1 .

III. TOPOLOGICAL MINI-BANDS IN MOIRÉ BHZ MODEL

In this section, we will discuss the BHZ model under a moiré superlattice potential and study its nontrivial band topology.

A. Moiré BHZ model and its symmetry property

The model Hamiltonian can be write as following

$$H = H_0 + H_M + H_R \quad (\text{S26})$$

$$H_0(k) = \epsilon(k)I + \begin{pmatrix} \mathcal{M}(k) & Ak_+ & 0 & 0 \\ Ak_- & -\mathcal{M}(k) & 0 & 0 \\ 0 & 0 & \mathcal{M}(k) & -Ak_- \\ 0 & 0 & -Ak_+ & -\mathcal{M}(k) \end{pmatrix} \quad (\text{S27})$$

$$H_R(k) = \begin{pmatrix} 0 & 0 & i\lambda k_- & 0 \\ 0 & 0 & 0 & 0 \\ -i\lambda k_+ & 0 & 0 & 0 \\ 0 & 0 & 0 & 0 \end{pmatrix} \quad (\text{S28})$$

$$H_M(\mathbf{r}) = \Delta_1 \sum_{\mathbf{g}} e^{i\mathbf{g}\cdot\mathbf{r}} I \quad (\text{S29})$$

with $k_\pm = k_x \pm ik_y$, $\mathcal{M}(k) = m - Bk^2$, $\epsilon(k) = -Dk^2$, and I is an identity matrix. The basis of above Hamiltonian are $|S, \uparrow\rangle, |P_+, \uparrow\rangle, |S, \downarrow\rangle$ and $|-P_-, \downarrow\rangle$, where P_\pm and S represent $P_x \pm P_y$ and S orbitals, respectively. The arrows

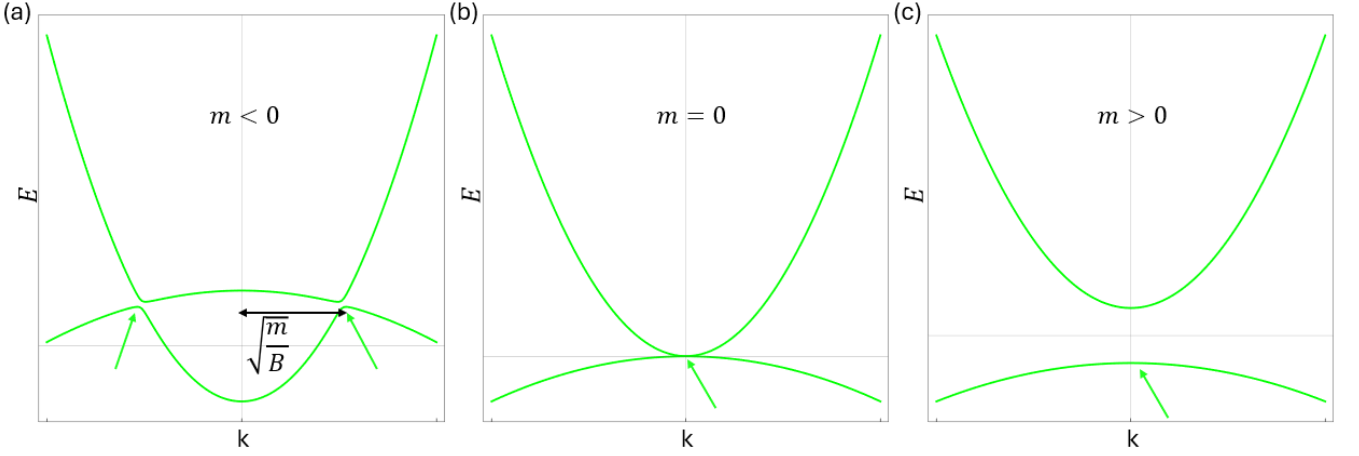


FIG. S4. (a)-(c) Band dispersions with $\Delta_1=0$, and $A = 0.01\text{nm}\cdot\text{eV}$. Here we choose a very small A value to illustrate why the valence band maximum is away from the Γ point. The green arrow points to the maximum of the valence band. When $m > 0$, the valence band maximum is at Γ . When $m = 0$, the valence band and conduction band touch at Γ . When $m < 0$, the valence band maximum is at $k = \sqrt{\frac{m}{B}}$ away from Γ .

\uparrow, \downarrow represent spin up and spin down, respectively. The H_0 term is the BHZ Hamiltonian [36]. $H_M(\mathbf{r})$ is the moiré potential, the summation of \mathbf{g} is as same as that in Eq.(2). The H_R term is Rashba SOC term. For the HgTe quantum wells, the material dependent parameters are given by $A = 0.365\text{nm}\cdot\text{eV}$, $B = -0.706\text{nm}^2\cdot\text{eV}$, and $D = -0.532\text{nm}\cdot\text{eV}$ [44]. For the moiré potential, we choose $|b_1^M| = \frac{\pi^2}{9\sqrt{3}}\text{nm}^{-1}$, so that the moiré unit cell length $L_m = 11.46\text{nm}$. We treat the gap parameter m , the Rashba SOC parameter λ and the moiré potential strength Δ_1 as tuning parameters. When both $\Delta_1 = 0$ $\lambda=0$ and $m < 0$, the valence band maximum can be away from Γ . In the weak coupling limit $A \rightarrow 0$, the valence band maximum is located around $k \sim \sqrt{\frac{m}{B}}$. Fig.S4 depicts the evolution of band dispersion for (a) negative, (b) zero and (c) positive m in the $A \rightarrow 0$ limit, respectively.

Below, we first consider Rashba SOC parameter $\lambda = 0$ and then discussion the case with nonzero λ .

The BHZ Hamiltonian H_0 in Eq.(S27) has the $D_{\infty h}$ symmetry, including the full rotation about z-axis, the mirror symmetries along the x, y, and z axis, denoted as \mathcal{M}_x , \mathcal{M}_y and \mathcal{M}_z , inversion symmetry \mathcal{I} , as well as the time reversal symmetry \mathcal{T} . With the moiré potential, the symmetry group of the Hamiltonian $H_0 + H_M$ is $P6/mmm$ that can be generated by \mathcal{M}_y , \mathcal{M}_z , six-fold rotation around the z-axis \mathcal{C}_{6z} , as well as \mathcal{T} . The inversion \mathcal{I} is also in this space group as $\mathcal{I} = \mathcal{M}_z\mathcal{C}_{6z}^3$. Because of \mathcal{T} and \mathcal{I} , all irreps in the group are doubly degenerate. Furthermore, due to the mirror \mathcal{M}_z , The Hamiltonian $H_0 + H_M$ can be written in a block diagonal with two blocks characterized by the opposite \mathcal{M}_z eigenvalue, namely, $\mathcal{M}_z = i$ for the upper block and $\mathcal{M}_z = -i$ for the lower block. The upper block Hamiltonian is written as

$$H_{upper}(k) = \begin{pmatrix} \mathcal{M}(k) + \epsilon(k) + \Delta_1 \sum_{\mathbf{g}} e^{i\mathbf{g}\cdot\mathbf{r}} & Ak_+ \\ Ak_- & -\mathcal{M}(k) + \epsilon(k) + \Delta_1 \sum_{\mathbf{g}} e^{i\mathbf{g}\cdot\mathbf{r}} \end{pmatrix}, \quad (\text{S30})$$

while the lower block H_{lower} can be related to H_{upper} by \mathcal{T} . The symmetry group for H_{upper} is described by magnetic space group $P6/mm'm'$ with the generators \mathcal{C}_{6z} , \mathcal{I} and $\mathcal{M}_y\mathcal{T}$. The symmetry group of H_{upper} turns out to be useful for our understanding of topological phase transitions discussed in Sec.B below. For the full Hamiltonian $H = H_0 + H_M + H_R$, in which the Rashba SOC H_R breaks both mirror \mathcal{M}_z and inversion \mathcal{I} , the symmetry group is further lowered to $P6mm$ with generators \mathcal{M}_y , \mathcal{C}_{6z} and \mathcal{T} .

B. Topological phase diagram of the moiré BHZ model with inversion symmetry

In the main text, we have discussed a variety of topological phases with different mirror Chern numbers and the corresponding topological phase transitions between them for the minibands VB1, which are mainly summarized in Fig. 3c of the main text. In particular, we focused on the phase transitions between moiré minibands from different momentum shells. In this section, we will provide more details on different topological phases and apply our moiré TQC formalism developed in Sec.I to understand the topological phase transition lines of VB1 around the weak moiré potential $\Delta_1 \rightarrow 0$ limit in Fig. 3c of the main text.

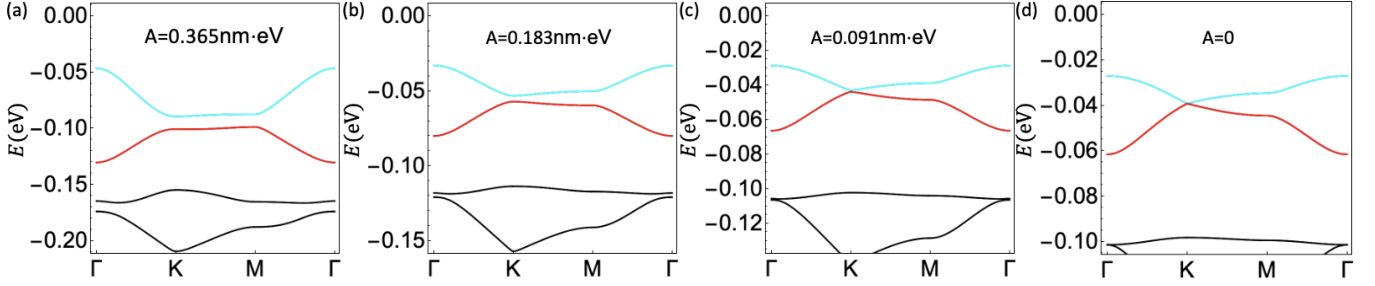


FIG. S5. (a)-(d) Band dispersions with $m=0.1\text{eV}$ and $\Delta_1 = -0.05\text{eV}$. The linear term A decrease from $0.365\text{nm}\cdot\text{eV}$ to 0 . The VB1 and VB2 are highlighted by cyan and right. VB1 is always separately in energy from the VB2 and the conduction bands when decreasing A from a large positive value to a very small positive one. The mini-gap between the VB1 and VB2 is closed at K when $A = 0$.

As discussed in the main text, the topological phase transitions in Fig. 3c involves the band inversion around Γ (green and black lines), M (yellow and red lines) and K (white line). These phase transition lines separate different topological phases for VB1, which can be characterized by the irreps of VB1 at high symmetry momenta, denoted by $(\bar{\Gamma}_i, \bar{K}_j, \bar{M}_k)$ or (i, j, k) for short. Below we will discuss these phase transition lines and the corresponding topological phases separately with the help of moiré TQC. We focus on the Hamiltonian $H_0 + H_M$ without the Rashba SOC H_R so that the inversion symmetry is preserved in this section and will discuss the influence of Rashba SOC H_R that breaks inversion symmetry in the next section.

Mapping the effective model in Region A to the Kane-Mele model

We start with the discussion of the non-trivial mirror Chern number in the region A. As the gap parameter m is positive in this region, the BHZ model H_0 is in the trivial phase by itself, and the nontrivial mirror Chern number comes from the influence of the moiré superlattice potential H_M . As we consider $\Delta_1 < 0$ in H_M , the valence bands feel a honeycomb lattice potential, so we expect our model here can be adiabatically connected to the Kane-Mele model, similar to the case of topological insulator thin film model in a honeycomb moiré superlattice studied in Ref.[87]. However, we notice that there is a difference in the basis wavefunctions between the BHZ model studied here and the TI thin film model studied in Ref. [87]. In the region A, the VB1 and the 2nd valence minibands, denoted as VB2, together form an EBR that corresponds to the orbitals with the angular momentum $J = \pm\frac{3}{2}$ in the honeycomb lattice. In contrast, the atomic orbitals with the angular momentum $J = \pm\frac{1}{2}$ appear in the honeycomb lattice in Ref.[87].

Non-trivial topology of this model in the regions with $m > 0$ and $\Delta_1 \rightarrow 0^-$ is guaranteed by the rotation eigenvalues at high symmetry momenta Γ , K and M in MBZ. The irreps of VB1 and VB2 at high symmetry point is $(\bar{\Gamma}_{10}, \bar{K}_8, \bar{M}_5)$ and $(\bar{\Gamma}_7, \bar{K}_9, \bar{M}_6)$, respectively. For the $M_z = +i$ block, the irreps of VB1 are $(\bar{\Gamma}_{13}^M, \bar{K}_{12}^M, \bar{M}_4^M)$, where we use \bar{k}_i^M to label the irrep of $P6/m'm'm$ at high symmetry point k . Because of C_6 symmetry, the Chern number of the $M_z = +i$ block is guaranteed to be $6n + 1$ with an integer n by the relation between the Chern number and the rotation eigen-values[88],

$$e^{iC\pi/3} = -\eta(\Gamma)\theta(K)\epsilon(M), \quad (\text{S31})$$

where $\theta(K)$, $\eta(\Gamma)$ and $\epsilon(M)$ represent the eigenvalues of C_{3z} at K , C_{6z} at Γ and C_{2z} at M , respectively. These rotation eigenvalues are completely determined by the irreps $(\bar{\Gamma}_{13}^M, \bar{K}_{12}^M, \bar{M}_4^M)$ of the $M_z = +i$ block for the VB1, which gives $\eta(\Gamma) = -i$, $\theta(K) = e^{i\frac{\pi}{3}}$ and $\epsilon(M) = -i$. The values of η, θ, ϵ for other irreps can be found in the Tab.S6, S7 and S8.

To show explicitly the adiabatic connection between our model $H_0 + H_M$ and the Kane-Mele model, we decrease the parameter value A for the linear term. As shown in the Fig.S5a-c, the VB1 is always separately in energy from the VB2 and the conduction bands when decreasing A from a large positive value to a very small positive one. In the $A \rightarrow 0^+$ limit, we can treat the linear term as a perturbation. At $A = 0$ (Fig.S5d), VB1 and VB2 are degenerate at K , giving rising to a Dirac cone, similar to the case of the graphene model. With a small A , we find the linear term can open a gap of the Dirac cone, leading to the effective model for both the VB1 at VB2 near K as

$$H_K^{eff}(k) = E_0(K) + \Delta_K \tau_0 \sigma_z + V_f(k_x \tau_z \sigma_x - k_y \tau_0 \sigma_y) \quad (\text{S32})$$

on the basis $|\frac{-1}{2}, +i\rangle, |\frac{1}{2}, +i\rangle, |\frac{1}{2}, -i\rangle$ and $|\frac{-1}{2}, -i\rangle$, where the basis function $|J, M_z\rangle$ is labelled by the eigen-values of symmetry operators C_{3z} and M_z as

$$C_{3z} |J, M_z\rangle = e^{-i\frac{2J\pi}{3}} |J, M_z\rangle; M_z |J, M_z\rangle = M_z |J, M_z\rangle. \quad (\text{S33})$$

$|\frac{-1}{2}, +i\rangle$ and $|\frac{1}{2}, -i\rangle$ form the irrep \bar{K}_8 , while $|\frac{-1}{2}, -i\rangle$ and $|\frac{1}{2}, +i\rangle$ form the irrep \bar{K}_9 . The Pauli matrices σ and τ are defined on the basis of M_z and C_{3z} eigen-states, respectively. The parameters in the effective model can be calculated from perturbation theory as

$$\begin{aligned} E_0(K) &= -DK^2 - \sqrt{A^2K^2 + \mathcal{M}(K)^2}; \\ V_f &= (-2D + \frac{-A^2 + 2BM}{\sqrt{A^2K^2 + \mathcal{M}(K)^2}})|K|; \\ \Delta_K &= \frac{(AK)^2}{2} \left(\frac{1}{-2\sqrt{A^2K^2 + \mathcal{M}(K)^2}} - \frac{1}{-2\sqrt{A^2K^2 + \mathcal{M}(K)^2} - 3\Delta_1} \right) \end{aligned} \quad (\text{S34})$$

The effective Hamiltonian in Eq.(S32) exactly takes the form of the Kane-Mele model near K .

Phase transition lines at Γ (green and black lines)

In the phase diagram Fig. 3c of the main text, there are two phase transition lines occurring at Γ (green and black lines). These two transitions, although both at Γ , have different physical origins. The transition of the green line occurs when the gap parameter m reverses its sign in the $\Delta_1 \rightarrow 0$ limit. Thus, this transition just corresponds to the band inversion of the original BHZ model H_0 . In the $\Delta_1 \rightarrow 0$, the irrep of VB1 at Γ is completely determined by H_0 . For $m > 0$, the irrep of VB1 is $\bar{\Gamma}_{10}$, while for $m < 0$, the irrep of VB1 is $\bar{\Gamma}_9$. Thus across the green line in the Fig.3c of the main text, the irrep of VB1 change from $\bar{\Gamma}_{10}$ in Region A to $\bar{\Gamma}_9$ in Region B, corresponding to a change of the mirror Chern number by 1, from $C_{\mathcal{M}} = 1$ in Region A to $C_{\mathcal{M}} = 2$ in Region B. The typical energy dispersion of mini-bands in Region A and B is shown in Fig.S9a and b, respectively.

The physical origin of the phase transition across the black line is because of the band inversion between the minibands from the 1st MBZ and those from the 2nd MBZ due to the band folding mechanism, as discussed in the main text. In the following, we will provide a band representation analysis of this phase transition line based on the moiré TQC, particularly illustrating the underlying reasons for the change of mirror Chern number by 2 across this transition line. Here we focus on the upper block H_{upper} in the $M_z = +i$ subspace, for which the eigen-states can be described by the irreps denoted by $\tilde{\Lambda}_k^M$ at the certain momentum k for the wave vector groups of magnetic space group $P6/mmm'$. At Γ , the wave vector group of $P6/mmm'$ is labelled by $6/mmm'$ with its character table shown in the Tab. S6 b and c according to the Bilbao Crystallographic Server[89–91].

As $6/mmm'$ is a subgroup of D_{6h} , all the irreps of D_{6h} can be decomposed into those of $6/mmm'$ from the Tab. S6 as

$$\begin{aligned} \bar{\Gamma}_7 &= \bar{\Gamma}_7^M \oplus \bar{\Gamma}_8^M; \bar{\Gamma}_8 = \bar{\Gamma}_9^M \oplus \bar{\Gamma}_{12}^M; \bar{\Gamma}_9 = \bar{\Gamma}_{10}^M \oplus \bar{\Gamma}_{11}^M; \\ \bar{\Gamma}_{10} &= \bar{\Gamma}_{13}^M \oplus \bar{\Gamma}_{14}^M; \bar{\Gamma}_{11} = \bar{\Gamma}_{15}^M \oplus \bar{\Gamma}_{18}^M; \bar{\Gamma}_{12} = \bar{\Gamma}_{16}^M \oplus \bar{\Gamma}_{17}^M. \end{aligned} \quad (\text{S35})$$

Two minibands with irrep $\bar{\Gamma}_i^M$ and $\bar{\Gamma}_j^M$, which are decomposed from the same $\bar{\Gamma}_i$, have different M_z eigenvalue and are degenerate. For the block H_{upper} , only $\bar{\Gamma}_8^M, \bar{\Gamma}_{10}^M, \bar{\Gamma}_{12}^M, \bar{\Gamma}_{13}^M, \bar{\Gamma}_{15}^M$ and $\bar{\Gamma}_{17}^M$ are relevant.

At the momentum shell \tilde{A}_Γ in the 1st MBZ, the four basis wavefunctions of H_0 belong to the irreps $\bar{\Gamma}_{10}$ and $\bar{\Gamma}_9$, or alternatively $\bar{\Gamma}_{13}^M$ and $\bar{\Gamma}_{10}^M$ for the upper block H_{upper} , respectively. The corresponding eigen-energies in small Δ limit are

$$E_\Gamma(\bar{\Gamma}_{10}^M) = m; \quad E_\Gamma(\bar{\Gamma}_{13}^M) = -m. \quad (\text{S36})$$

We next consider the 6 momenta in the momentum shell \tilde{A}_{Γ^1} in the 2nd MBZ and focus on the upper block H_{upper} in Eq.(S30). For zero Δ_1 , at each momentum in the ABZ, there are two eigen-states with the eigen-energies

$$E_\pm(k) = -Dk^2 \pm \sqrt{Ak^2 + \mathcal{M}^2(k)}, \quad (\text{S37})$$

where \pm represent the conduction and valence bands, respectively. The corresponding eigen-wave functions are labelled as $|\pm, k, M_z = i\rangle$ or abbreviated as $|\pm, k, i\rangle$. Here we only focus on the lower energy eigen-states for the

(a)

D_{6h}	ε	C_{3z}, C_{3z}^{-1}	C_{2z}	C_{6z}, C_{6z}^{-1}	$C_{2x}, C_{3z}C_{2x}, C_{3z}^{-1}C_{2x}$	$C_{2y}, C_{3z}C_{2y}, C_{3z}^{-1}C_{2y}$	J	$\bar{C}_{3z}, \bar{C}_{3z}^{-1}$	\mathcal{M}_{001}	$\bar{C}_{6z}, \bar{C}_{6z}^{-1}$	$\mathcal{M}_{110}, \mathcal{M}_{100}, \mathcal{M}_{010}$	$\mathcal{M}_{1\bar{1}0}, \mathcal{M}_{120}, \mathcal{M}_{210}$
$\bar{\Gamma}_7$	2	-2	0	0	0	0	2	-2	0	0	0	0
$\bar{\Gamma}_8$	2	1	0	$-\sqrt{3}$	0	0	2	1	0	$-\sqrt{3}$	0	0
$\bar{\Gamma}_9$	2	1	0	$\sqrt{3}$	0	0	2	1	0	$\sqrt{3}$	0	0
$\bar{\Gamma}_{10}$	2	-2	0	0	0	0	-2	2	0	0	0	0
$\bar{\Gamma}_{11}$	2	1	0	$-\sqrt{3}$	0	0	-2	-1	0	$\sqrt{3}$	0	0
$\bar{\Gamma}_{12}$	2	1	0	$\sqrt{3}$	0	0	-2	-1	0	$-\sqrt{3}$	0	0

(b)

$6/m\bar{m}'m'$	ε	C_{3z}	C_{3z}^{-1}	C_{2z}	C_{6z}^{-1}	C_{6z}	J	\bar{C}_{3z}	\bar{C}_{3z}^{-1}	\mathcal{M}_{001}	\bar{C}_{6z}	\bar{C}_{6z}^{-1}
$\bar{\Gamma}_8^M$	1	-1	-1	-i	-i	i	1	-1	-1	i	-i	i
$\bar{\Gamma}_{10}^M$	1	$e^{-i\pi/3}$	$e^{i\pi/3}$	-i	$e^{i\pi/6}$	$e^{-i\pi/6}$	1	$e^{-i\pi/3}$	$e^{i\pi/3}$	i	$e^{i\pi/6}$	$e^{-i\pi/6}$
$\bar{\Gamma}_{12}^M$	1	$e^{i\pi/3}$	$e^{-i\pi/3}$	-i	$e^{i5\pi/6}$	$e^{-i5\pi/6}$	1	$e^{i\pi/3}$	$e^{-i\pi/3}$	i	$e^{i5\pi/6}$	$e^{-i5\pi/6}$
$\bar{\Gamma}_{13}^M$	1	-1	-1	i	i	-i	-1	1	1	i	-i	i
$\bar{\Gamma}_{15}^M$	1	$e^{-i\pi/3}$	$e^{i\pi/3}$	i	$e^{-i5\pi/6}$	$e^{i5\pi/6}$	-1	$e^{i2\pi/3}$	$e^{-i2\pi/3}$	i	$e^{i\pi/6}$	$e^{-i\pi/6}$
$\bar{\Gamma}_{17}^M$	1	$e^{i\pi/3}$	$e^{-i\pi/3}$	i	$e^{-i\pi/6}$	$e^{i\pi/6}$	-1	$e^{-i2\pi/3}$	$e^{i2\pi/3}$	i	$e^{i5\pi/6}$	$e^{-i5\pi/6}$

(c)

$6/m\bar{m}'m'$	ε	C_{3z}	C_{3z}^{-1}	C_{2z}	C_{6z}^{-1}	C_{6z}	J	\bar{C}_{3z}	\bar{C}_{3z}^{-1}	\mathcal{M}_{001}	\bar{C}_{6z}	\bar{C}_{6z}^{-1}
$\bar{\Gamma}_7^M$	1	-1	-1	i	i	-i	1	-1	-1	-i	i	-i
$\bar{\Gamma}_9^M$	1	$e^{-i\pi/3}$	$e^{i\pi/3}$	i	$e^{-i5\pi/6}$	$e^{i5\pi/6}$	1	$e^{-i\pi/3}$	$e^{i\pi/3}$	-i	$e^{-i5\pi/6}$	$e^{i5\pi/6}$
$\bar{\Gamma}_{11}^M$	1	$e^{i\pi/3}$	$e^{-i\pi/3}$	i	$e^{-i\pi/6}$	$e^{i\pi/6}$	1	$e^{i\pi/3}$	$e^{-i\pi/3}$	-i	$e^{-i\pi/6}$	$e^{i\pi/6}$
$\bar{\Gamma}_{14}^M$	1	-1	-1	-i	-i	i	-1	1	1	-i	i	-i
$\bar{\Gamma}_{16}^M$	1	$e^{-i\pi/3}$	$e^{i\pi/3}$	-i	$e^{i\pi/6}$	$e^{-i\pi/6}$	-1	$e^{i2\pi/3}$	$e^{-i2\pi/3}$	-i	$e^{-i5\pi/6}$	$e^{i5\pi/6}$
$\bar{\Gamma}_{18}^M$	1	$e^{i\pi/3}$	$e^{-i\pi/3}$	-i	$e^{i5\pi/6}$	$e^{-i5\pi/6}$	-1	$e^{-i2\pi/3}$	$e^{i2\pi/3}$	-i	$e^{i\pi/6}$	$e^{-i\pi/6}$

TABLE S6. (a) The character table for the wave vector group D_{6h} . (b)-(c) The character table of the unitary symmetry operations in wave vector group $6/m\bar{m}'m'$. In the irrep listed in (b), $M_z = i$, while in the irrep listed in (c), $M_z = -i$.

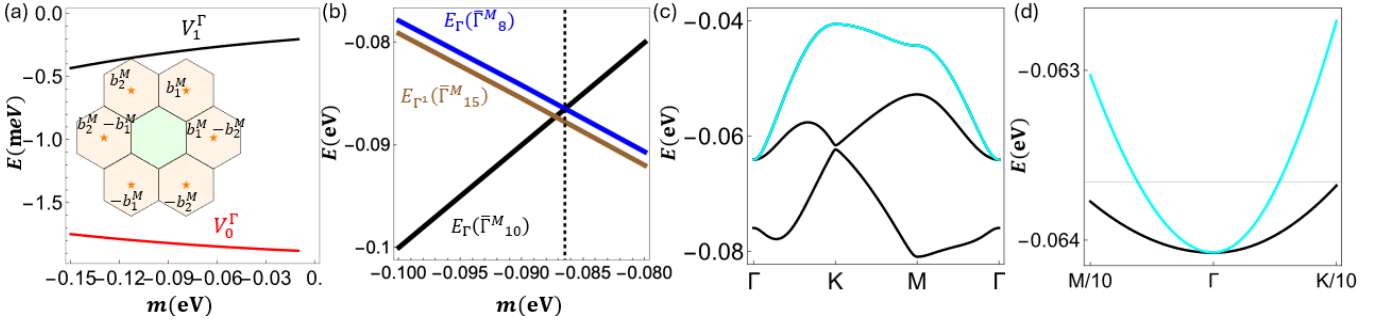


FIG. S6. (a) The value of V_1^Γ as a function of m at $\Delta_1 = -0.002\text{eV}$. The insert shows the momenta in the \tilde{A}_{Γ^1} (b) $E_\Gamma(\bar{\Gamma}_{10}^M)$, $E_{\Gamma^1}(\bar{\Gamma}_{15}^M)$ and $E_{\Gamma^1}(\bar{\Gamma}_8^M)$ near the transition line at $\Delta_1 = -0.002\text{eV}$ (c) Band dispersion at the black line. (d) Band dispersion near the Γ point of (c). The band touching at the Γ point is quadratic.

valence bands at 6 momenta in \tilde{A}_{Γ^1} , $|-, b_1^M - b_2^M, i\rangle, |-, b_1^M, i\rangle, |-, b_2^M, i\rangle, |-, b_2^M - b_1^M, i\rangle, |-, -b_1^M, i\rangle, |-, -b_2^M, i\rangle$, and denote the corresponding representation as $\tilde{\Lambda}_{\Gamma^1}^M$. On the basis of these 6 wave functions, the representation matrices for C_{6z} , \mathcal{I} and $M_y\mathcal{T}$ operators have the forms

$$C_{6z}(\tilde{\Lambda}_{\Gamma^1}^M) = \begin{pmatrix} 0 & 0 & 0 & 0 & 0 & -i \\ -i & 0 & 0 & 0 & 0 & 0 \\ 0 & -i & 0 & 0 & 0 & 0 \\ 0 & 0 & -i & 0 & 0 & 0 \\ 0 & 0 & 0 & -i & 0 & 0 \\ 0 & 0 & 0 & 0 & -i & 0 \end{pmatrix}; \mathcal{I}(\tilde{\Lambda}_{\Gamma^1}^M) = \begin{pmatrix} 0 & 0 & 0 & -1 & 0 & 0 \\ 0 & 0 & 0 & 0 & -1 & 0 \\ 0 & 0 & 0 & 0 & 0 & -1 \\ -1 & 0 & 0 & 0 & 0 & 0 \\ 0 & -1 & 0 & 0 & 0 & 0 \\ 0 & 0 & -1 & 0 & 0 & 0 \end{pmatrix}; M_y\mathcal{T}(\tilde{\Lambda}_{\Gamma^1}^M) = \begin{pmatrix} 0 & 0 & 0 & 1 & 0 & 0 \\ 0 & 0 & 1 & 0 & 0 & 0 \\ 0 & 1 & 0 & 0 & 0 & 0 \\ 1 & 0 & 0 & 0 & 0 & 0 \\ 0 & 0 & 0 & 0 & 0 & 1 \\ 0 & 0 & 0 & 0 & 1 & 0 \end{pmatrix}. \quad (\text{S38})$$

The representation $\tilde{\Lambda}_{\Gamma^1}^M$ is reducible, and based on the representation matrices and the character table Tab.S6, we find

$$\tilde{\Lambda}_{\Gamma^1}^M = \bar{\Gamma}_8^M \oplus \bar{\Gamma}_{10}^M \oplus \bar{\Gamma}_{12}^M \oplus \bar{\Gamma}_{13}^M \oplus \bar{\Gamma}_{15}^M \oplus \bar{\Gamma}_{17}^M \quad (\text{S39})$$

By considering the first order perturbation for the Moiré potential H_M , we derive the form of the effective model

on these 6 eigen-state basis as

$$\mathcal{H}(\Gamma^1) = \begin{pmatrix} E_-(b_1^M) & V_0^\Gamma + iV_1^\Gamma & 0 & 0 & 0 & V_0^\Gamma - iV_1^\Gamma \\ V_0^\Gamma - iV_1^\Gamma & E_-(b_1^M) & V_0^\Gamma + iV_1^\Gamma & 0 & 0 & 0 \\ 0 & V_0^\Gamma - iV_1^\Gamma & E_-(b_1^M) & V_0^\Gamma + iV_1^\Gamma & 0 & 0 \\ 0 & 0 & V_0^\Gamma - iV_1^\Gamma & E_-(b_1^M) & V_0^\Gamma + iV_1^\Gamma & 0 \\ 0 & 0 & 0 & V_0^\Gamma - iV_1^\Gamma & E_-(b_1^M) & V_0^\Gamma + iV_1^\Gamma \\ V_0^\Gamma + iV_1^\Gamma & 0 & 0 & 0 & V_0^\Gamma - iV_1^\Gamma & E_-(b_1^M) \end{pmatrix}, \quad (\text{S40})$$

where $E_-(b_1^M)$ is obtained from Eq.(S37). The coupling term V_i^Γ is defined as following:

$$V_0^\Gamma = \text{Re}(\Delta_1 \langle -, b_1^M, i | -, b_2^M, i \rangle); V_1^\Gamma = \text{Im}(\Delta_1 \langle -, b_1^M, i | -, b_2^M, i \rangle). \quad (\text{S41})$$

This Hamiltonian satisfies the symmetry properties,

$$C_{6z}(\tilde{\Lambda}_{\Gamma^1}^M)\mathcal{H}(\Gamma^1)C_{6z}^{-1}(\tilde{\Lambda}_{\Gamma^1}^M) = \mathcal{H}(\Gamma^1); \mathcal{I}(\tilde{\Lambda}_{\Gamma^1}^M)\mathcal{H}(\Gamma^1)\mathcal{I}^{-1}(\tilde{\Lambda}_{\Gamma^1}^M) = \mathcal{H}(\tilde{\Lambda}_{\Gamma^1}^M); M_y\mathcal{T}(\tilde{\Lambda}_{\Gamma^1}^M)\mathcal{H}(\Gamma^1)(M_y\mathcal{T})^{-1}(\tilde{\Lambda}_{\Gamma^1}^M) = \mathcal{H}^*(\Gamma^1). \quad (\text{S42})$$

Unlike the coupling term in Eq.(S18) that only depend on Δ_1 , V_0^Γ and V_1^Γ also depends on the parameters $M, B, A, |b_1^M|$.

The energies of \mathcal{H}_{Γ^1} are

$$\begin{aligned} E_{\Gamma^1}(\bar{\Gamma}_{17}^M) &= E(\Gamma^1) - V_0^\Gamma + \sqrt{3}V_1^\Gamma; E_{\Gamma^1}(\bar{\Gamma}_{15}^M) = E(\Gamma^1) - V_0^\Gamma - \sqrt{3}V_1^\Gamma; E_{\Gamma^1}(\bar{\Gamma}_8^M) = E(\Gamma^1) - 2V_0^\Gamma; \\ E_{\Gamma^1}(\bar{\Gamma}_{10}^M) &= E(\Gamma^1) + V_0^\Gamma + \sqrt{3}V_1^\Gamma; E_{\Gamma^1}(\bar{\Gamma}_{12}^M) = E(\Gamma^1) + V_0^\Gamma - \sqrt{3}V_1^\Gamma; E_{\Gamma^1}(\bar{\Gamma}_{13}^M) = E(\Gamma^1) + 2V_0^\Gamma; \end{aligned} \quad (\text{S43})$$

Fig. S6a shows V_0^Γ and V_1^Γ as a function of m at $\Delta_1 = -0.002\text{eV}$, and Fig. S6b shows the eigen-energies of the $\bar{\Gamma}_8^M$ and $\bar{\Gamma}_{15}^M$ states in Eq.(S43) from \tilde{A}_{Γ^1} and the $\bar{\Gamma}_{10}^M$ states in Eq.(S36) from \tilde{A}_Γ as a function of the gap parameter m . One can see a band crossing between the $\bar{\Gamma}_{10}^M$ and $\bar{\Gamma}_8^M$ states at $m = -0.0865\text{eV}$, so the VB1 belong to the irrep $\bar{\Gamma}_8^M$ for $m < -0.0865\text{eV}$ and $\bar{\Gamma}_{10}^M$ for $m > -0.0865\text{eV}$. We notice that the C_{6z} rotation eigen-values for the irreps $\bar{\Gamma}_{10}^M$ and $\bar{\Gamma}_8^M$ are $e^{-i\frac{\pi}{6}}$ and $+i$ respectively, so the band touching at the transition point has a quadratic form, as shown in in the Fig.S6c and d, and the mirror Chern number C_M is changed by 2 according to Eq.(S31).

In the above, we have discussed the irreps of VB1 for the upper block Hamiltonian H_{upper} , while in the main text, we use the irreps of the full Hamiltonian $H_0 + H_M$. The correspondence can be read out from the decomposition forms in Eq.(S35), from which the decomposition of the irreps for the momentum shell \tilde{A}_{Γ^1} can be given by

$$\tilde{\Lambda}_{\Gamma^1} = \bar{\Gamma}_7 \oplus \bar{\Gamma}_8 \oplus \bar{\Gamma}_9 \oplus \bar{\Gamma}_{10} \oplus \bar{\Gamma}_{11} \oplus \bar{\Gamma}_{12} \quad (\text{S44})$$

for the full Hamiltonian. Moreover, the transition between $\bar{\Gamma}_{10}^M$ and $\bar{\Gamma}_{13}^M$ corresponds to that between $\bar{\Gamma}_9$ and $\bar{\Gamma}_{10}$ for the full Hamiltonian, according to Eq.(S35). This transition is illustrated by the green line in Fig.3c. The transition between $\bar{\Gamma}_{10}^M$ and $\bar{\Gamma}_{13}^M$ corresponds to that between $\bar{\Gamma}_9$ and $\bar{\Gamma}_7$, which is illustrated by the black line in Fig.3c.

Phase transition lines at M (yellow and red lines)

In this section, we analyze the yellow and red transition lines at high-symmetry momentum M , which is described by the wave vector group D_{2h} . Here we again only consider the upper block Hamiltonian H_{upper} ($M_z = +i$) that is described by the magnetic little group $mm'm'$ with generators \mathcal{I} , $M_y\mathcal{T}$ and M_z . For the wave vector group D_{2h} , the double group irreps are \bar{M}_5 and \bar{M}_6 , which can be decomposed into the irreps of $mm'm'$ as

$$\bar{M}_5 = \bar{M}_3^M \oplus \bar{M}_4^M; \bar{M}_6 = \bar{M}_5^M \oplus \bar{M}_6^M. \quad (\text{S45})$$

For $M_z = +i$ sector (H_{upper} block), the relevant irreps are \bar{M}_4^M and \bar{M}_5^M .

We label the 1st and 2nd momentum shells for M as \tilde{A}_M and \tilde{A}_{M^1} , respectively, which are given by

$$\begin{aligned} \tilde{A}_M &= \{b_1^M/2, -b_1^M/2\} \\ \tilde{A}_{M^1} &= \{b_1^M/2 - b_2^M, -b_1^M/2 + b_2^M\}, \end{aligned} \quad (\text{S46})$$

as shown in the inset of Fig.S7a.

Here we consider the effective model on both momentum shells \tilde{A}_M and \tilde{A}_{M^1} together, and the corresponding basis wave functions are labelled by $|-, b_1^M/2, i\rangle$ and $|-, -b_1^M/2, i\rangle$ for the irrep $\tilde{\Lambda}_M$ at \tilde{A}_M and $|-, -b_1^M/2 + b_2^M, i\rangle$ and

$|-, b_1^M/2 - b_2^M, i\rangle$ for the irrep $\tilde{\Lambda}_{M^1}$ at \tilde{A}_{M^1} . The matrix representations of the \mathcal{I} and $M_y\mathcal{T}$ operators at these basis wave functions can be written as

$$\mathcal{I}(\tilde{\Lambda}_M^M \oplus \tilde{\Lambda}_{M^1}^M) = \begin{pmatrix} 0 & -1 & 0 & 0 \\ -1 & 0 & 0 & 0 \\ 0 & 0 & 0 & -1 \\ 0 & 0 & -1 & 0 \end{pmatrix}; M_y\mathcal{T}(\tilde{\Lambda}_M^M \oplus \tilde{\Lambda}_{M^1}^M) = \begin{pmatrix} 0 & 1 & 0 & 0 \\ 1 & 0 & 0 & 0 \\ 0 & 0 & 1 & 0 \\ 0 & 0 & 0 & 1 \end{pmatrix}. \quad (\text{S47})$$

The representation $\tilde{\Lambda}_{M^1}^M$ and $\tilde{\Lambda}_M^M$ are reducible, and can be decomposed into the irreps of the magnetic little group $mm'm'$ as

$$\tilde{\Lambda}_M^M = \bar{M}_4^M \oplus \bar{M}_5^M; \tilde{\Lambda}_{M^1}^M = \bar{M}_4^M \oplus \bar{M}_5^M, \quad (\text{S48})$$

based on the representation matrices and the character table in Tab.S7.

By considering the lowest order perturbation for the Moiré potential H_M , we derive the form of the effective model on these 4 eigen-states as

$$\mathcal{H}(M \oplus M^1) = \begin{pmatrix} E_-(b_1^M/2) & V_0^M & V_1^M + iV_2^M & V_1^M - iV_2^M \\ V_0^M & E_-(b_1^M/2) & V_1^M - iV_2^M & V_1^M + iV_2^M \\ V_1^M - iV_2^M & V_1^M + iV_2^M & E_-(b_1^M/2 - b_2^M) & 0 \\ V_1^M + iV_2^M & V_1^M - iV_2^M & 0 & E_-(b_1^M/2 - b_2^M) \end{pmatrix}; \quad (\text{S49})$$

where

$$V_0^M = \Delta_1 \langle -, -b_1^M/2, i | -, b_1^M/2, i \rangle, \\ V_1^M = \text{Re} (\Delta_1 \langle -, b_1^M/2 - b_2^M, i | -, b_1^M/2, i \rangle); V_2^M = \text{Im} (\Delta_1 \langle -, b_1^M/2 - b_2^M, i | -, b_1^M/2, i \rangle). \quad (\text{S50})$$

This Hamiltonian satisfies the symmetry requirements

$$\mathcal{I}(\tilde{\Lambda}_M^M \oplus \tilde{\Lambda}_{M^1}^M) \mathcal{H}(M \oplus M^1) \mathcal{I}^{-1}(\tilde{\Lambda}_M^M \oplus \tilde{\Lambda}_{M^1}^M) = \mathcal{H}(M \oplus M^1); \quad (\text{S51})$$

$$M_y\mathcal{T}(\tilde{\Lambda}_M^M \oplus \tilde{\Lambda}_{M^1}^M) \mathcal{H}(M \oplus M^1) (M_y\mathcal{T})^{-1}(\tilde{\Lambda}_M^M \oplus \tilde{\Lambda}_{M^1}^M) = \mathcal{H}^*(M \oplus M^1). \quad (\text{S52})$$

The eigen-energies of \mathcal{H}_M up to the lowest order perturbation are

$$E_M(\bar{M}_5^M) = E_-(b_1^M/2) + V_0^M; E_{M^1}(\bar{M}_5^M) = E_-(b_1^M/2 - b_2^M) + \frac{(V_1^M)^2}{E_-(b_1^M/2) - E_-(b_1^M/2)} \\ E_M(\bar{M}_4^M) = E_-(b_1^M/2) - V_0^M; E_{M^1}(\bar{M}_4^M) = E_-(b_1^M/2 - b_2^M) + \frac{(V_2^M)^2}{E_-(b_1^M/2) - E_-(b_1^M/2)}, \quad (\text{S53})$$

where the energy $E_-(k)$ is obtained from Eq.(S37) for the momentum k .

For a positive or small negative m ($m > -0.104\text{eV}$), we find $E(M) > E(M^1)$ and the VB1 comes from the first momentum shell \tilde{A}_M and thus we only need to compare the eigen-energies $E_M(\bar{M}_5^M)$ and $E_M(\bar{M}_4^M)$ in Eq.(S53). The sign of V_0^M depends on m and reverses from negative to positive at $m = -0.071\text{eV}$ when decreasing m , as shown in the Fig.S7a. Thus, the VB1 carries the irrep \bar{M}_4^M for $m > -0.071\text{eV}$ and the irrep \bar{M}_5^M for $m < -0.071\text{eV}$, following the Eq.(S53) and shown in Fig. S7c.

When $m < -0.104\text{eV}$, the minibands from the second momentum shell \tilde{A}_{M^1} have lower energy, so the irrep of VB1 at M depends on the miniband eigen-energies of $E_{M^1}(\bar{M}_5^M)$ and $E_{M^1}(\bar{M}_4^M)$. Fig. S7b depicts the amplitudes $|V_2^M|$ and $|V_1^M|$ as a function of m at $\Delta_1 = -0.002\text{eV}$, in which we find $|V_2^M| < |V_1^M|$ for $m > -0.123\text{eV}$ and $|V_2^M| > |V_1^M|$ for $m < -0.123\text{eV}$. Therefore, the irrep for the VB1 is also changed at $m = -0.123\text{eV}$ according to Eq.(S53). It belongs to \bar{M}_5^M for $m > -0.123\text{eV}$ and \bar{M}_4^M for $m < -0.123\text{eV}$, as shown in Fig. Fig. S7d.

Combining all the discussions above, we find the VB1 belongs to the irrep \bar{M}_5^M for $-0.123\text{eV} < m < -0.071\text{eV}$ and \bar{M}_4^M for $m > -0.071\text{eV}$ or $m < -0.123\text{eV}$.

The above analysis of irreps can be extended to the full Hamiltonian. According to Eq.(S45), the irreps of the eigen-states in the momentum shells \tilde{A}_M and \tilde{A}_{M^1} for the full Hamiltonian are

$$\tilde{\Lambda}_M = \bar{M}_5 \oplus \bar{M}_6; \tilde{\Lambda}_{M^1} = \bar{M}_5 \oplus \bar{M}_6. \quad (\text{S54})$$

According to Eq.(S45), the transition between \bar{M}_5^M and \bar{M}_4^M corresponds to that between \bar{M}_6 and \bar{M}_5 for the full Hamiltonian. The transition near $m = -0.071\text{eV}$ ($m = -0.123\text{eV}$) corresponds to the yellow (black) line in Fig.3c of the main text. It is noted that both two transitions are between \bar{M}_6 and \bar{M}_5 are within the same momentum shell.

(a)

D_{2h}	\mathcal{E}	\mathcal{C}_{2z}	\mathcal{C}_{2x}	\mathcal{C}_{2y}	\mathcal{J}	\mathcal{M}_{100}	\mathcal{M}_{010}	\mathcal{M}_{001}
\bar{M}_5	2	0	0	0	2	0	0	0
\bar{M}_6	2	0	0	0	-2	0	0	0

(b)

$mm'm'$	\mathcal{E}	\mathcal{C}_{2z}	\mathcal{J}	\mathcal{M}_{001}
\bar{M}_4^M	2	-i	1	i
\bar{M}_5^M	2	i	-1	i

(c)

$mm'm'$	\mathcal{E}	\mathcal{C}_{2z}	\mathcal{J}	\mathcal{M}_{001}
\bar{M}_3^M	2	i	1	-i
\bar{M}_6^M	2	-i	-1	-i

TABLE S7. (a) The character table for the wave vector group D_{2h} . (b)-(c) The character table of the unitary symmetry operations in wave vector group $mm'm'$. In the irrep listed in (b), $M_z = i$, while in the irrep listed in (c), $M_z = -i$.

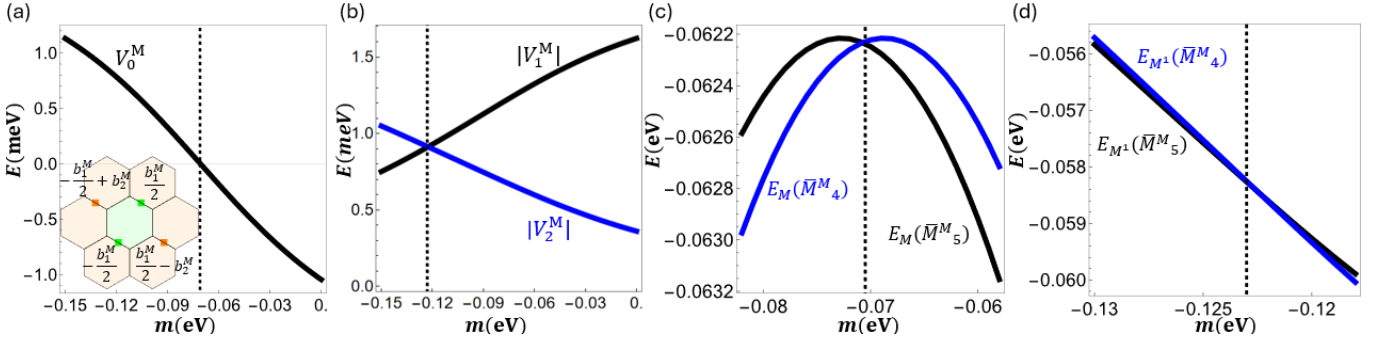


FIG. S7. (a) The value of V_0^M as a function of m at $\Delta_1 = -0.002\text{eV}$. The insert shows the momenta in \bar{A}_M and \bar{A}_{M1} (b) The value of $|V_1^M|$ and $|V_2^M|$ as a function of m at $\Delta_1 = -0.002\text{eV}$. (c) $E_M(\bar{M}_4^M)$, $E_M(\bar{M}_5^M)$ near the yellow line at $\Delta_1 = -0.002\text{eV}$ (d) $E_M(\bar{M}_4^M)$, $E_M(\bar{M}_5^M)$ near the red line at $\Delta_1 = -0.006\text{eV}$

(a)

D_{3h}	\mathcal{E}	$\mathcal{C}_{3z}, \mathcal{C}_{3z}^{-1}$	$\bar{\mathcal{C}}_{6z}^{-1}, \bar{\mathcal{C}}_{6z}$	$\mathcal{C}_{2y}, \mathcal{C}_{3z}\mathcal{C}_{2y}, \mathcal{C}_{3z}^{-1}\mathcal{C}_{2y}$	$\mathcal{M}_{1\bar{1}0}, \mathcal{M}_{120}, \mathcal{M}_{210}$	\mathcal{M}_{001}
\bar{K}_7	2	-2	0	0	0	0
\bar{K}_8	2	1	$-\sqrt{3}$	0	0	0
\bar{K}_9	2	1	$\sqrt{3}$	0	0	0

(b)

$\bar{6}m'2'$	\mathcal{E}	\mathcal{C}_{3z}	\mathcal{C}_{3z}^{-1}	$\bar{\mathcal{C}}_{6z}$	$\bar{\mathcal{C}}_{6z}^{-1}$	\mathcal{M}_{001}
\bar{K}_8^M	1	-1	-1	i	-i	i
\bar{K}_{10}^M	1	$e^{-i\pi/3}$	$e^{i\pi/3}$	$e^{-i\pi/6}$	$e^{i\pi/6}$	i
\bar{K}_{12}^M	1	$e^{i\pi/3}$	$e^{-i\pi/3}$	$e^{-i5\pi/6}$	$e^{i5\pi/6}$	i

(c)

$\bar{6}m'2'$	\mathcal{E}	\mathcal{C}_{3z}	\mathcal{C}_{3z}^{-1}	$\bar{\mathcal{C}}_{6z}$	$\bar{\mathcal{C}}_{6z}^{-1}$	\mathcal{M}_{001}
\bar{K}_8^M	1	-1	-1	-i	i	-i
\bar{K}_{10}^M	1	$e^{-i\pi/3}$	$e^{i\pi/3}$	$e^{i5\pi/6}$	$e^{-i5\pi/6}$	-i
\bar{K}_{12}^M	1	$e^{i\pi/3}$	$e^{-i\pi/3}$	$e^{i\pi/6}$	$e^{-i\pi/6}$	-i

TABLE S8. (a) The character table for the wave vector group D_{3h} . (b)-(c) The character table of the unitary symmetry operations in wave vector group $\bar{6}m'2'$. In the irrep listed in (b), $M_z = i$, while in the irrep listed in (c), $M_z = -i$.

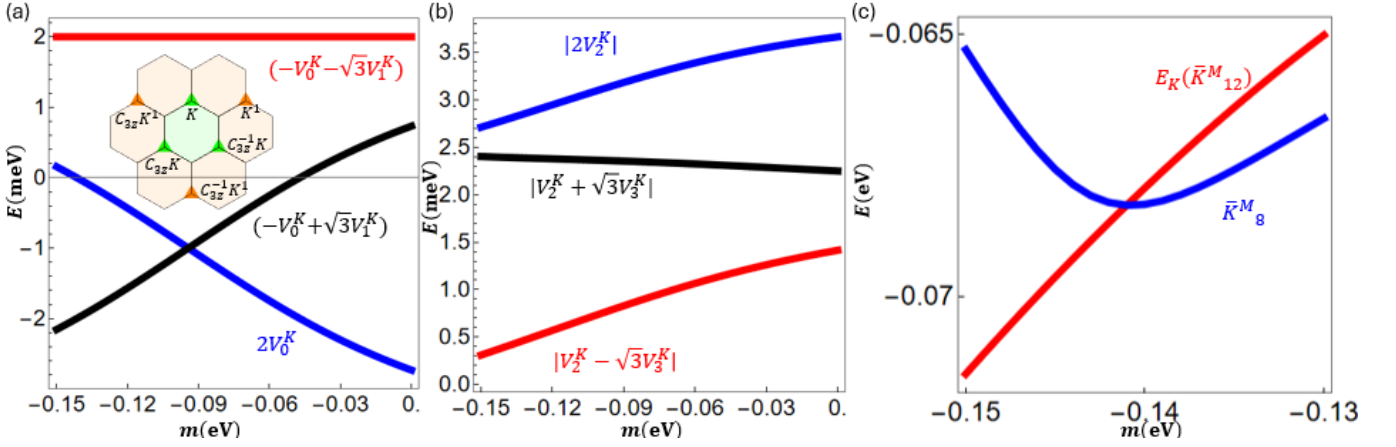


FIG. S8. (a) The value of $2V_0^K$, $-V_0^K + \sqrt{3}V_1^K$ and $-V_0^K - \sqrt{3}V_1^K$ as a function of m at $\Delta = -0.002\text{eV}$. The insert shows the momentum in the \tilde{A}_K and \tilde{A}_{K^1} (b) The value of $2|V_2^K|$, $|V_2^K + \sqrt{3}V_3^K|$ and $|V_2^K - \sqrt{3}V_3^K|$ as a function of m at $\Delta = -0.002\text{eV}$. (c) The energy of \bar{K}_{12}^M , and \bar{K}_8^M states near the transition line at $\Delta_1 = -0.002\text{eV}$.

Phase transition line at K (white line)

In this section, we analyze the white transition lines at high-symmetry momentum K in Fig.3c of the main text. The wave vector group at K is described by the point group D_{3h} for the full Hamiltonian $H_0 + H_M$, and the upper block Hamiltonian H_{upper} ($M_z = +i$) is described by the magnetic little group $\bar{6}m'2'$ with generators M_z , $M_y T$ and \mathcal{IC}_{6z} . For the wave vector group D_{3h} , the double group irreps are \bar{K}_7 , \bar{K}_8 and \bar{K}_9 , which can be decomposed into the irreps of $\bar{6}m'2'$ as

$$\bar{K}_7 = \bar{K}_7^M \oplus \bar{K}_8^M; \bar{K}_8 = \bar{K}_9^M \oplus \bar{K}_{12}^M; \bar{K}_9 = \bar{K}_{10}^M \oplus \bar{K}_{11}^M. \quad (\text{S55})$$

For $M_z = +i$ sector (H_{upper} block), the relevant irreps are \bar{K}_8^M , \bar{K}_{10}^M and \bar{K}_{12}^M .

Here we consider the effective model on both momentum shells \tilde{A}_K and \tilde{A}_{K^1} in Eq.(S12) together, and the corresponding basis wave functions are labelled by $|-, K, i\rangle$, $|-, C_{3z}K, i\rangle$ and $|-, C_{3z}^{-1}K, i\rangle$ for the irrep $\tilde{\Lambda}_K$ at \tilde{A}_K and $|-, C_{3z}^{-1}K^1, i\rangle$, $|-, K^1, i\rangle$ and $|-, C_{3z}K^1, i\rangle$ for the irrep $\tilde{\Lambda}_{K^1}$ at \tilde{A}_{K^1} .

The matrix representations of \mathcal{IC}_{6z} $M_y \mathcal{T}$ operators on these basis can be written as

$$\mathcal{IC}_{6z}(\tilde{\Lambda}_K \oplus \tilde{\Lambda}_{K^1}) = \begin{pmatrix} 0 & i & 0 & 0 & 0 & 0 \\ 0 & 0 & i & 0 & 0 & 0 \\ i & 0 & 0 & 0 & 0 & 0 \\ 0 & 0 & 0 & 0 & i & 0 \\ 0 & 0 & 0 & 0 & 0 & i \\ 0 & 0 & 0 & i & 0 & 0 \end{pmatrix}; M_y \mathcal{T}(\tilde{\Lambda}_K \oplus \tilde{\Lambda}_{K^1}) = \begin{pmatrix} 1 & 0 & 0 & 0 & 0 & 0 \\ 0 & 0 & 1 & 0 & 0 & 0 \\ 0 & 1 & 0 & 0 & 0 & 0 \\ 0 & 0 & 0 & 1 & 0 & 0 \\ 0 & 0 & 0 & 0 & 0 & 1 \\ 0 & 0 & 0 & 1 & 0 & 0 \end{pmatrix}. \quad (\text{S56})$$

From the representation matrices and the character table Tab.S8, we find the representation $\tilde{\Lambda}_K^M$ and $\tilde{\Lambda}_{K^1}^M$ can be decomposed by

$$\tilde{\Lambda}_K^M = \bar{K}_8^M \oplus \bar{K}_{10}^M \oplus \bar{K}_9^M; \tilde{\Lambda}_{K^1}^M = \bar{K}_8^M \oplus \bar{K}_{10}^M \oplus \bar{K}_9^M. \quad (\text{S57})$$

The effective model on these eigen-state basis as is derived as

$$\mathcal{H}(K \oplus K^1) = \begin{pmatrix} E_-(K) & V_0^K + iV_1^K & V_0^K - iV_1^K & 0 & V_2^K - iV_3^K & V_2^K + iV_3^K \\ V_0^K - iV_1^K & E_-(K) & V_0^K + iV_1^K & V_2^K + iV_3^K & 0 & V_2^K - iV_3^K \\ V_0^K + iV_1^K & V_0^K - iV_1^K & E_-(K) & V_2^K - iV_3^K & V_2^K + iV_3^K & 0 \\ 0 & V_2^K - iV_3^K & V_2^K + iV_3^K & E_-(K^1) & 0 & 0 \\ V_2^K + iV_3^K & 0 & V_2^K - iV_3^K & 0 & E_-(K^1) & 0 \\ V_2^K - iV_3^K & V_2^K + iV_3^K & 0 & 0 & 0 & E_-(K^1) \end{pmatrix}. \quad (\text{S58})$$

where

$$\begin{aligned} V_0^K &= \Delta_1 \text{Re} \langle -, K, i | -, C_{3z}^{-1}K, i \rangle; V_1^K = \Delta_1 \text{Im} \langle -, K, i | -, C_{3z}^{-1}K, i \rangle, \\ V_2^K &= \Delta_1 \text{Re} \langle -, K^1, i | -, K, i \rangle; V_3^K = \Delta_1 \text{Im} \langle -, K^1, i | -, K, i \rangle, \end{aligned} \quad (\text{S59})$$

and the energies $E_-(K)$ and $E_-(K^1)$ can be obtained from Eq.(S37). This Hamiltonian satisfies

$$\mathcal{I}C_{6z}(\tilde{\Lambda}_K \oplus \tilde{\Lambda}_{K^1})\mathcal{H}(K \oplus K^1)(\mathcal{I}C_{6z})^{-1}(\tilde{\Lambda}_K \oplus \tilde{\Lambda}_{K^1}) = \mathcal{H}(K \oplus K^1); \quad (\text{S60})$$

$$M_y\mathcal{T}(\tilde{\Lambda}_K \oplus \tilde{\Lambda}_{K^1})\mathcal{H}(K \oplus K^1)(M_y\mathcal{T})^{-1}(\tilde{\Lambda}_K \oplus \tilde{\Lambda}_{K^1}) = \mathcal{H}^*(K \oplus K^1). \quad (\text{S61})$$

The eigen-energies of the above effective Hamiltonian \mathcal{H}_K can be derived perturbatively as

$$\begin{aligned} E_K(\bar{K}_8^M) &= E_-(K) + 2V_0^K; E_{K^1}(\bar{K}_8^M) = E_-(K^1) + \frac{(2V_2^K)^2}{E_-(K^1) - E_-(K)}, \\ E_K(\bar{K}_{10}^M) &= E_-(K) - V_0^K + \sqrt{3}V_1^K; E_{K^1}(\bar{K}_{10}^M) = E_-(K^1) + \frac{(V_2^K + \sqrt{3}V_3^K)^2}{E_-(K^1) - E_-(K)}, \\ E_K(\bar{K}_{12}^M) &= E_-(K) - V_0^K - \sqrt{3}V_1^K; E_{K^1}(\bar{K}_{12}^M) = E_-(K^1) + \frac{(V_2^K - \sqrt{3}V_3^K)^2}{E_-(K^1) - E_-(K)}, \end{aligned} \quad (\text{S62})$$

where the energy $E_-(k)$ is obtained from Eq.(S37) for the momentum k .

When $E_-(K) > E_-(K^1)$, we compare three eigen-energies $E_K(\bar{K}_8^M)$, $E_K(\bar{K}_{10}^M)$ and $E_K(\bar{K}_{12}^M)$. Fig.S8a shows $2V_0^K$, $-V_0^K + \sqrt{3}V_1^K$ and $-V_0^K - \sqrt{3}V_1^K$ as a function of m at $\Delta = -0.002\text{eV}$. From Eq. (S62), we always find the \bar{K}_{12}^M state has largest energy.

When band inversion of minibands between the first and 2nd momentum shells happens at K point ($E_-(K) < E_-(K^1)$) for $m < -0.142\text{eV}$, the irrep of VB1 at K depend on the energy ordering of $E_{K^1}(\bar{K}_8^M)$, $E_{K^1}(\bar{K}_{10}^M)$ and $E_{K^1}(\bar{K}_{12}^M)$. Fig.S8b shows $2|V_2^K|$, $|V_2^K + \sqrt{3}V_3^K|$ and $|V_2^K - \sqrt{3}V_3^K|$ as a function of m at $\Delta = -0.002\text{eV}$. From Eq. (S62), we find $E_{K^1}(\bar{K}_8^M)$ is the largest one. Thus, the band crossing occurs between the \bar{K}_8^M states from \tilde{A}_{K^1} and the \bar{K}_{12}^M states from \tilde{A}_K at $m = -0.142\text{eV}$, as shown in Fig.S8c. The VB1 belongs to the irrep \bar{K}_8^M for $m < -0.142\text{eV}$ and \bar{K}_{12}^M for $m > -0.142\text{eV}$.

The above analysis of irreps can be extended to the full Hamiltonian. According to Eq.(S55), the irreps at the momentum shells \tilde{A}_K and \tilde{A}_{K^1} for the full Hamiltonian are

$$\tilde{\Lambda}_K = \bar{K}_7 \oplus \bar{K}_8 \oplus \bar{K}_9; \tilde{\Lambda}_{K^1} = \bar{K}_7 \oplus \bar{K}_8 \oplus \bar{K}_9. \quad (\text{S63})$$

The transition between \bar{K}_8^M and \bar{K}_{12}^M corresponds to that between \bar{K}_7 and \bar{K}_8 for the full Hamiltonian, according to Eq.(S55), which corresponds to the white line in Fig.3c of the main text.

Miniband dispersion and topologically nontrivial flat minibands

In the main text, we have shown the energy dispersion of the minibands in the region D and E to illustrate the band inversion at Γ due to the band-folding mechanism. In Fig.S9, we show the typical energy dispersion for the minibands, particularly the VB1, in the other regions in the phase diagram (Fig. 3c of the main text). Fig.S9a-c correspond region A-C, and Fig.S9d-f correspond region F-H in Fig.3c of the main text.

Generally, we find the minibands of VB1 are dispersive and exhibit a small energy mini-gap from other minibands. To extract more energy dispersion information for VB1, we depict the bandwidth of the VB1, the mini-band gap between the VB1 and the conduction minibands, and the mini-band gap between the VB1 and VB2 in Fig.S10(a), (b) and (c), respectively. An interesting observation is that at the crosses d and e labelled in Fig.S10(a), the bandwidth of VB1 is locally minimized while a significant mini-band gap exists between the VB1 and VB2, as well as between the VB1 and conduction minibands. The energy dispersion for the VB1 is depicted in Fig.S10(d) and (e) for the parameters at the crosses d and e in S10(a). The mirror Chern numbers of the VB1 for the point d and e are -1 and 1, respectively. Thus, the topologically nontrivial flat minibands of the VB1 in these two regions are identified and can potentially support fractional Chern insulator phase. This was very recently discussed in details in Ref.[60].

C. Topological phase diagram of the moiré BHZ model without inversion symmetry

Topological phase diagram without inversion

In this section, we will consider the topological phase diagram for the VB1 with the full Hamiltonian H in Eq. (S26) without inversion. We choose a small Rashba SOC term so that there is no additional band closing between VB1 and other bands. As the Rashba SOC term reduces the symmetry group from $P6/mmm$ to $P6mm$, the mirror

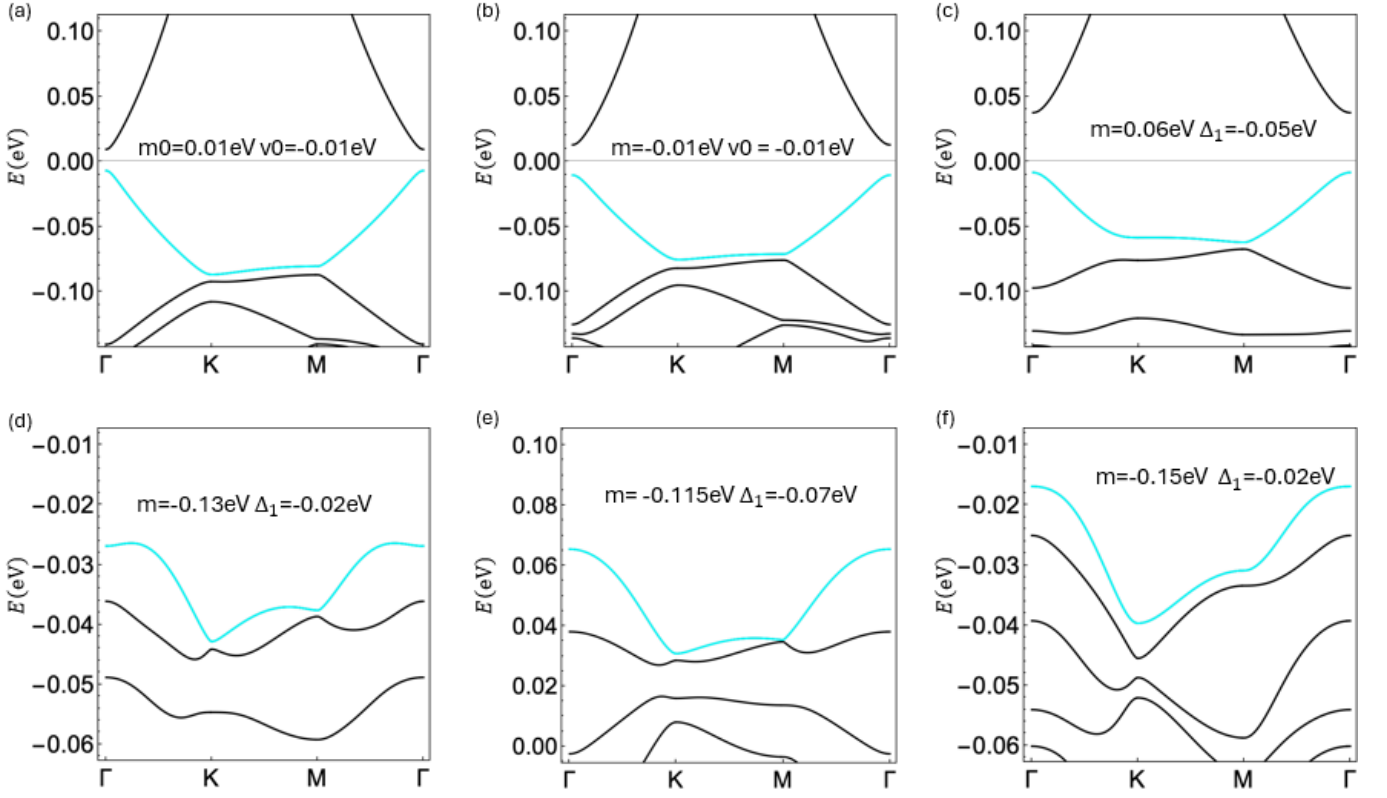


FIG. S9. (a)-(c) band dispersions in the region A-C in the Fig.4C in the main text. (d)-(f) band dispersions in the region F-H in the Fig.4C in the main text.

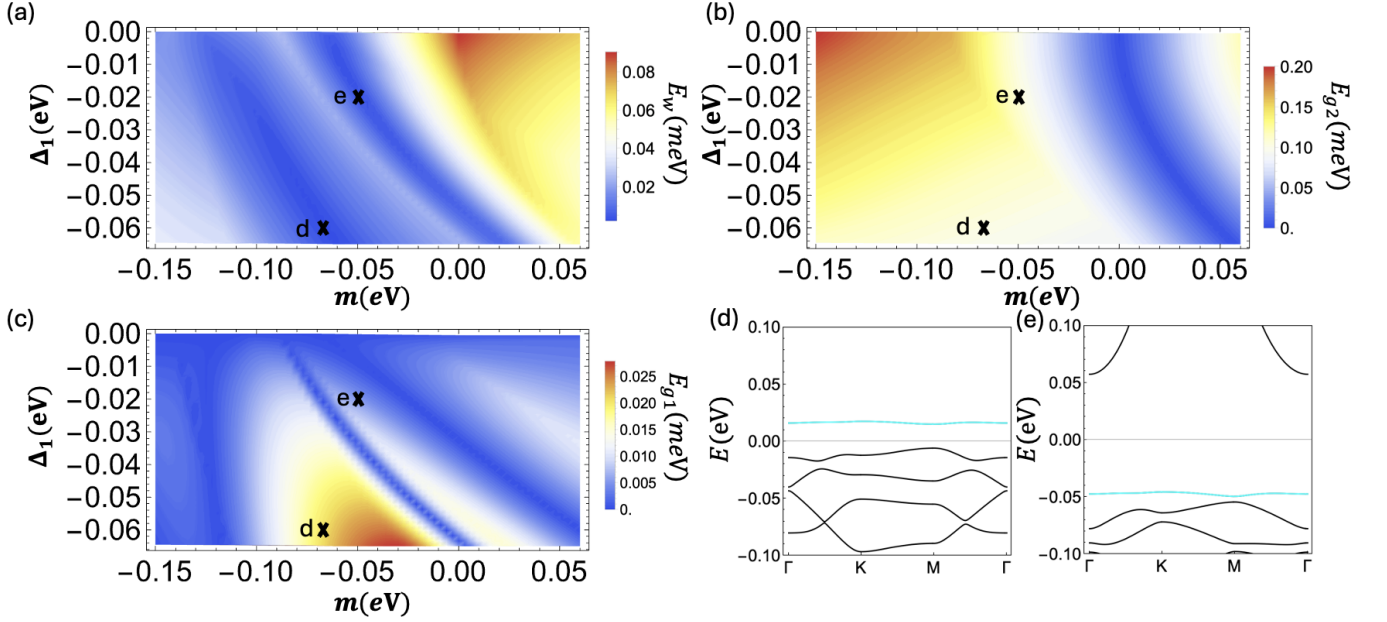


FIG. S10. (a) Bandwidth E_w of VB1 as function of Δ_1 and m . (b) The band gap between VB1 and CB1 E_{g2} as function of Δ_1 and m . (c) The band gap between VB1 and VB2 E_{g1} as function of Δ_1 and m . (d)-(e) The band dispersion with parameters labeled by the cross in a.

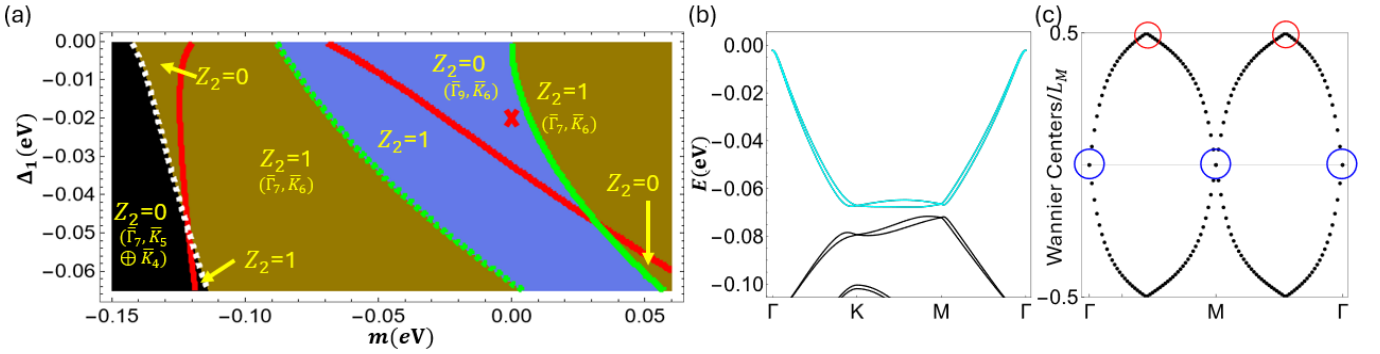


FIG. S11. (a) Topological phase diagram of VB1 without inversion symmetry. Different color distinguish irreps at high symmetry points. The solid lines identify Z_2 number change. The green solid lines separate regions with different irreps. The dashed lines identify irrep change meanwhile Z_2 number does not change. (a) Band dispersion with Rashba SOC strength $\lambda=0.02\text{eV}$. and parameters labeled by the red cross in (a). (b) Wannier center flow for VB1. The Wannier center flow still reveals a double winding feature when Rashba SOC is included. The crossings labeled by blue circles at Γ and M are protected by \mathcal{T} and the crossings labeled by red circles are protected by $C_{2z}\mathcal{T}$ symmetry.

Chern number is no longer well defined. However, due to the existence of time reversal symmetry, Z_2 number is still valid, which can be connected to the mirror Chern number by $\nu = C_{\mathcal{M}} \bmod 2$. Therefore, all the phases with odd mirror Chern number for the VB1 in the phase diagram of Fig. 3c in the main text will also be Z_2 non-trivial in the phase diagram after breaking the inversion as shown in Fig.S11(a). We also label the band irreps of VB1 at high symmetry momenta, which can be obtained from the compatibility relations discussed in the character table in Tab.S2,S3,S6-S8. In this figure, two green lines and one white dashed line, separate regions with different irreps. Those three lines correspond to the green, black and white solid lines in the Fig.3c of the main text. However, the irreps changes are not always accompanied by a Z_2 number change. Among these three lines, the Z_2 number is only change across the solid green line. In addition, there are another two solid red lines in Fig.S11(a) that changes the Z_2 number although the band irreps do not change across these lines. These two red solid lines correspond to yellow and red solid lines in the Fig.3c of the main text.

For the $C_{\mathcal{M}} = \pm 2$ phase in the regions B, C and F of Fig.3c of the main text, the Z_2 number is 0, which suggests these two regions should be trivial after taking into account the Rashba SOC term H_R . However, as we will discuss below, this is *not* true and the model shows the fragile topology that is protected by the $C_{2z}\mathcal{T}$ symmetry in these two regions after including the Rashba SOC term that breaks inversion.

Fragile topology in the regions B

We take the region B as an example. The band dispersion and the Wannier center flow for the VB1, denoted as $\theta(k)$, are shown in Fig.S11b and c, respectively. The Wannier center flow $\theta(k)$ for the VB1 reveals a double winding feature, implying the non-trivial band topology in this region. To illustrate the stability of this double winding feature, we examine the symmetry protection of the crossing points in the Wannier center flow, as depicted by two red and three blue circles in Fig.S11c. The crossing points at three blue circles are at time-reversal invariant momenta Γ and M , and thus protected by the \mathcal{T} symmetry. The crossings at two red circles are stabilized by the $C_{2z}\mathcal{T}$ symmetry. The $C_{2z}\mathcal{T}$ symmetry operator does not change the momentum k , but will reverse the Wannier center θ . Thus, the $C_{2z}\mathcal{T}$ symmetry requires the spectrum of Wannier center flow to be symmetric with respect to $\theta = 0$ (or equivalently $\theta = 0.5$). Furthermore, $C_{2z}\mathcal{T}$ guarantees that the crossings at $\theta = 1/2$, as depicted by the red circles in Fig.S11c, can only move in the $\theta = 1/2$ line, but not be gapped. To see that, we consider the Wilson Hamiltonian, defined by $H_W = \frac{1}{2\pi i} \log(\mathcal{W}(k))$, where $\mathcal{W}(k)$ is the Wilson loop [54]. The eigen-values of $H_W(k)$ describes the Wannier center flow $\theta(k)$. The $C_{2z}\mathcal{T}$ symmetry of the Wilson loop $\mathcal{W}(k)$ requires the anti-commutation relation between $C_{2z}\mathcal{T}$ and H_W , as it flips the Wannier center[58]. Now we consider the expansion of the Wilson Hamiltonian around the red crossing point at $1/2$ in Fig.S11c, which takes the form $H_W(\delta k) = \delta k \sigma_z$, where δk is the momentum away from the crossing point. The above Wilson Hamiltonian anti-commutes with $C_{2z}\mathcal{T} = \sigma_x K$ where K is complex conjugation and we have used the fact that one should define the Wannier center flow θ module 1 so that $\theta = 1/2$ is equivalent to $\theta = -1/2$. Now we will show that $C_{2z}\mathcal{T}$ symmetry can stabilize the crossing at $\theta = 1/2$. We consider certain perturbation Hamiltonian $\delta H_W = \sum_{i=x,y,z} \delta_i \sigma_i$. The anti-commutation relation between $C_{2z}\mathcal{T}$ symmetry and δH_W requires $\delta_x = \delta_y = 0$. Thus, one can see that the remaining δ_z term can only shift the crossing point to $k = -\delta_z$ for

the Wilson Hamiltonian $H_W + \delta H_W$. Thus, we prove the local stability of the crossing at $\theta = 1/2$.

The double winding of $\theta(k)$ indicates that the VB1 in the region B cannot be adiabatically connected to the atomic limit so that the VB1 is non-trivial. Next we will demonstrate that the VB1 carries fragile topology by trivializing the Wannier center flow of the VB1 with adding additional trivial bands. The band representation of the VB1 is $(\bar{\Gamma}_9, \bar{K}_6, \bar{M}_5)$. By inspecting the EBR of the space group $P6mm$ [89–91], we find the band representation of the VB1 can be combined with an EBR $\bar{E}_2 \uparrow G(2)@1a$ with $(\bar{\Gamma}_8, \bar{K}_6, \bar{M}_5)$ and an EBR $\bar{E}_3 \uparrow G(2)@1a$ with $(\bar{\Gamma}_7, \bar{K}_4 \oplus \bar{K}_5, \bar{M}_5)$ to make an EBR $\bar{E}_3 \uparrow G(6)@3c$ with $(\bar{\Gamma}_9 \oplus \bar{\Gamma}_7 \oplus \bar{\Gamma}_8, \bar{K}_4 \oplus \bar{K}_5 \oplus 2\bar{K}_6, 3\bar{M}_5)$. Therefore, we can consider the following Hamiltonian

$$H_{combine}(k) = \begin{pmatrix} H(m, \Delta_1, \lambda) & 0 & 0 \\ 0 & H_T & 0 \\ 0 & 0 & \epsilon_2 + H(m', \Delta'_1, \lambda') \end{pmatrix} + H_{int}(k) \quad (\text{S64})$$

$$H_{int}(k) = \begin{pmatrix} 0 & H_{I1}(k) & H_{I2}(k) \\ H_{I1}^\dagger(k) & 0 & 0 \\ H_{I2}^\dagger(k) & 0 & 0 \end{pmatrix} \quad (\text{S65})$$

$$H_T = (\epsilon_1 + \alpha k^2 + \Delta_1'' \sum_{\mathbf{g}} e^{i\mathbf{g}\cdot\mathbf{r}}) I \quad (\text{S66})$$

$$H_{I1}(k) = V_{int}^0 \begin{pmatrix} 0 & (k_x + ik_y)^2 \\ i(k_x + ik_y)^2 & (k_x + ik_y) \\ (k_x - ik_y)^2 & 0 \\ (-k_x + ik_y) & i(k_x - ik_y)^2 \end{pmatrix} \quad (\text{S67})$$

$$H_{I2}(k) = V_{int}^1 I, \quad (\text{S68})$$

where I represents a 4-by-4 identity matrix. $H(m, \Delta, \lambda)$ is Moiré BHZ model in Eq.(S26) with the gap parameter m , the moiré potential Δ_1 and the Rashba SOC parameter λ . The form of the coupling Hamiltonian H_{int} is derived from the requirements of preserving the \mathcal{M}_y , \mathcal{C}_{6z} and \mathcal{T} symmetries. Here the parameters are chosen to make the VB1 of the Hamiltonian $H(m, \Delta, \lambda)$ in the region B of the phase diagram in Fig.3c of the main text, and other parameters are chosen as $\epsilon_1=0.015\text{eV}$, $\epsilon_2=-0.05\text{eV}$, $\alpha=0.1nm^2\cdot\text{eV}$, $V_{int}^0=0.1nm\cdot\text{eV}$, $V_{int}^1=0.004\text{eV}$, $\Delta_1''=-0.01\text{eV}$, $\Delta_1'=-0.06\text{eV}$, $m'=0.1\text{eV}$ and $\lambda'=0.4nm\cdot\text{eV}$. The TB1 minibands (See Fig.S12a) from the Hamiltonian $H(m', \Delta', \lambda')$ to possess the band representation $(\bar{\Gamma}_7, \bar{K}_4 \oplus \bar{K}_5)$, and the TB2 minibands (See Fig.S12a) from the Hamiltonian H_T belonging to the band representation $(\bar{\Gamma}_8, \bar{K}_6)$. The full band dispersion of the model $H_{combine}$ is shown in the Fig.S12a. The $\theta(k)$ for the TB1 and TB2 in Fig.S12b exhibits a trivial feature. The $\theta(k)$ for the VB1 of the Hamiltonian $H_{combine}$ still reveals a double winding feature in the Fig.S12c, and thus the band topology of the VB1 remains the same. By including two additional trivial bands of TB1 and TB2 in the calculation of Wannier center flow, as shown in the Fig.S12d and e, we find the overall Wannier center flow $\theta(k)$ for all three minibands, the VB1, TB1 and TB2, are fully gapped and become trivial. Therefore, we demonstrate that the doubling winding of the VB1 in region B of Fig.3c of the main text can be gapped out by introducing trivial bands, thus belonging to the fragile topology.

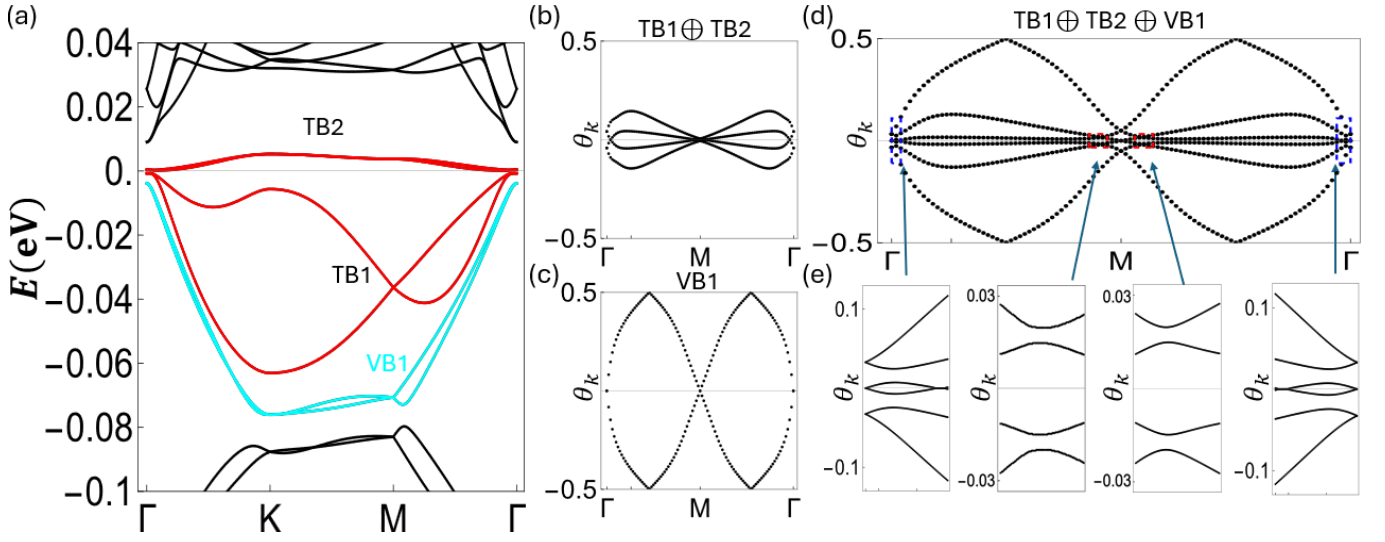


FIG. S12. (a) Band dispersion, when 2 trivial bands highlighted by Red are included. The irrep of VB1 is $(\bar{\Gamma}_9, \bar{K}_6)$, the irrep of TB1 is $(\bar{\Gamma}_7, \bar{K}_4 \oplus \bar{K}_5)$, and the irrep of TB2 is $(\bar{\Gamma}_8, \bar{K}_6)$ (b) Wannier center flow for two 2 trivial bands (c) Wannier center flow for VB1. (d) Wannier center flow for VB1 and two trivial bands. (e) Zoom in Wannier center flow in the dashed box in d. By including two trivial bands, we can gap out the Wannier center flow